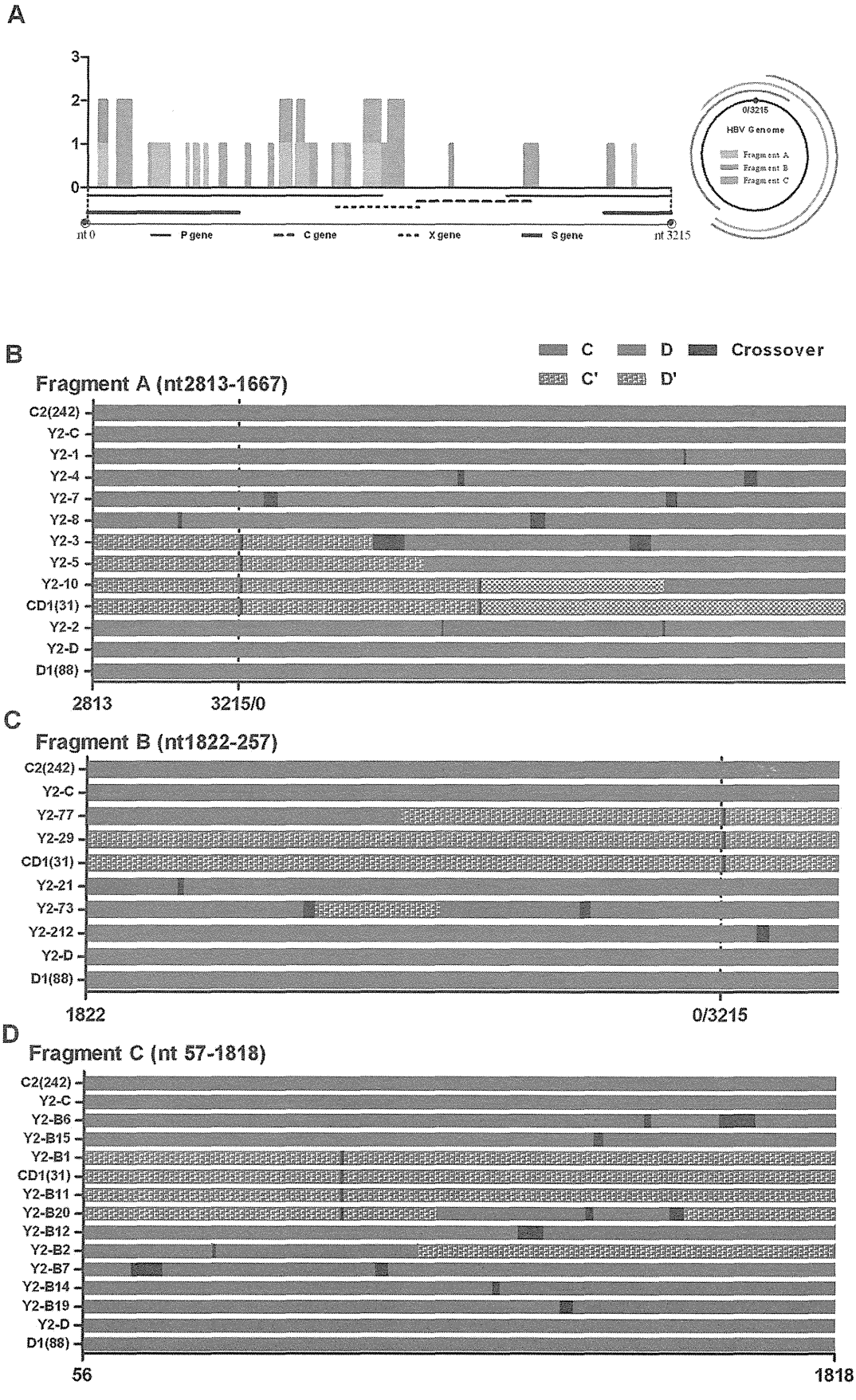
A
3
2
1
0
nt 0
P gene
C gene
X gene
S gene
nt 3215
0/3215
HBV Genome
Fragment A
Fragment B
Fragment C
B
C
D
Crossover
C'
D'
Fragment A (nt2813-1667)
C2(242)
Y2-C
Y2-1
Y2-4
Y2-7
Y2-8
Y2-3
Y2-5
Y2-10
CD1(31)
Y2-2
Y2-D
D1(88)
2813
3215/0
C
Fragment B (nt1822-257)
C2(242)
Y2-C
Y2-77
Y2-29
CD1(31)
Y2-21
Y2-73
Y2-212
Y2-D
D1(88)
1822
0/3215
D
Fragment C (nt 57-1818)
C2(242)
Y2-C
Y2-B6
Y2-B15
Y2-B1
CD1(31)
Y2-B11
Y2-B20
Y2-B12
Y2-B2
Y2-B7
Y2-B14
Y2-B19
Y2-D
D1(88)
56
1818

Figure 3. Alignment and recombination crossover regions found in Y2 clones. (**A**) Frequency and distribution of the recombination crossover regions found in Y2 clones along the HBV genome. The bars indicate the number of clones (y axis) showing recombination crossover regions at each site. The 1-3215 of x axis was consistent with the nt1-3215 of HBV genome. Different colors represent the sites find from clones of different PCR region: pink bars for fragment A, grey bars for fragment B and green bars for fragment C. (**B**) Alignment of fragment A (HBV nt 2813-0-1667). Y2-1′12: clones from fragment A of Y2 patients. (**C**) Alignment of fragment B (HBV nt 1822-0-257). Y2-21′212: clones from fragment B of Y2 patients. (**D**) Alignment of fragment C (HBV nt 57-1818) of Y2 clones. Y2-B1′B22: clones from fragment C of Y2 patients. The number on the x axis was consistent with the site of nucleotides of HBV genome. Solid green lines are genotype C2, solid pink lines are genotype D1, speckled green lines are the C2 component of genotype recombinant CD1 and speckled pink lines are the D1 component of recombinant genotype CD1. The black lines are sequence that is common to the recombining genotypes, and within which the recombination probably occurred. C2 (242) is the consensus sequence formed by 242 subgenotype C2 sequences from GenBank. D1 (88) is the consensus sequence formed by 88 subgenotype D1 sequences from GenBank. CD1 (33) is the consensus sequence formed by CD1 recombinant sequences from GenBank.
doi:10.1371/journal.pone.0038241.g003

suggests C2 and D1 are parental sequences of CD1 and CD2 recombinants. Virological differences among HBV genotypes were demonstrated in vitroand in CHiM mice, with genotype C having a higher replication capacity than D [23]. Why does the replication-deficient genotype D virus predominate over replication-competent genotype C? As mixed HBV infections together with recombination are rare, we have little knowledge about i this situation. On the one hand, we know little about host impact on different genotypes and recombinants. On the other hand, we know little about interference and competition in the quasi-species of mixed infection. In vitro results showed the replication capacity of individual clone, exclude the influence of host and other strains of quasi-species. An example from a ChiM mice study showed that monoinfection of HBV/G in ChiM mice display a very slow replication while coinfection with HBV/A remarkably enhanced the replication of HBV/G. The replication of HBV/G is heavily dependent on coinfection with other genotypes. When HBV/G superinfected on other genotypes, a rapidly takes over of HBV/G from original genotype were observed, though they are indispensable [24]. This study confirms that in a mixed infection system of different genotypes, the replication capacity of a genotype may be different from that of monoinfection. At the same time, replication capacity is not the only factor to influence which strain will become dominant. Variable recombinants found in our study may be mechanistically capable of genetic exchange, but strong selection guaranteed the elimination of hybrid genomes. The mechanism of selection in mixed infection also needs more investigation.

We found mixed HBV genotypes infection with many novel recombinants at one point in time, but just one genotype was found 18 months later. This may indicate that the detectable mixed infection and recombination has a limited time window due to the sensitivity of detection or strong selection power of the host. That's why in most studies, we can identify a major genotype in one patient. Even so, evolutionarily visible and invisible recombination of HBV could occur and play an important role by generating genetic variation or reducing mutational load. However, this study had limitation, because recombination signals were detected by RDP3 software and confirmed by split phylogenetic tree and alignment, indicating the recombinant or recombinant-like form should depend on the software. If we use another software, the results might be different.

Studies of HBV in endemic areas throughout the world have resulted in large numbers of full genome sequences available for phylogenetic analysis enabling the identification of novel, mosaic HBV genomes that appear to be the result of recombination between previously known sequences [7,25,26]. One of the most comprehensive analyses of putative HBV inter-genotype recombinants showed the existence of 24 phylogenetically independent HBV genomes involving all known human genotypes [27]. Some of these recombinants are unique to individual subjects, but some undergo expansion in specific populations and become recognized as new genotypes or subgenotypes [12,28,29,30]. Four stages in the process of generating popular HBV recombinant genomes should be recognized. The first stage is the co-circulation of different HBV strains or genotypes in the same geographic area. The second is the existence of individuals who have been infected with more than one strain of HBV. The third is the generation of a novel recombinant strain(s) within an individual. The fourth is the selection of a recombined strain with the ability to replicate and be transmitted. Our data show the natural process of the formation and selection of recombination though the recombinant strains of Y2 that appeared in 2006 that were all removed from samples in 2007.

By using phylogenetic trees and homology calculations, HBV variants infecting humans are currently classified into ten genotypes that differ from each other in nucleotide sequence by 7.5 to 13% [2,3]. There are some characteristic length differences between the genotypes that facilitates their detection and discrimination. However, as shown in Figure 2, existence of a recombinant makes the topology of the phylogenetic tree totally different from one with no recombinant. Recombinant strains obscured the definition of genotypes. Based on the algorithm creating a phylogenetic tree, sequences with high homologues cluster together. With the same logic, recombinants always clustered with the backbone parental sequence, in other words, with which they have high similarity with the larger proportion of the recombination region. Therefore, recombinants always seem to be a subgenotype of their backbone parental sequence. Similar to Y2-8 clone in Figure 2C, for recombinants with similar proportion of both parental genotypes, the sequence shows a divergent trend different from both parental genotypes.

Based on phylogenetic topology changes of different regions of HBV, it was hypothesized that some of the genotypes that are conventionally regarded as "pure," actually were recombinant. Genotype E strains show evidence of recombination with genotype D at 1950–2500. new reported genotype "I" actually belongs to genotype C. Furthermore, Subgenotype Ba possesses the recombination with genotype C at 1740 to 2485 [31,32,33]. Recombinants comprising regions with different histories have important implications for the way we think about HBV evolution. It means that there is no single phylogenetic tree that can describe the evolutionary relationships between genotypes.

In conclusion, mixed HBV genotypes infection with many novel recombinants at one point in time ended up with just one genotype 18 months later in this study. This may indicate that the detectable mixed infection and recombination have a limited time window due to the sensitivity of detection or strong selection power of the host. Also, as the recombinant or recombinant-like nature of HBV precludes the possibility of a "true" phylogenetic taxonomy, a new standard may be required for classifying HBV sequences.

Supporting Information

Figure S1 Recombination map of fragment A created by RDP software.
(TIF)

Figure S2 Recombination map of fragment B created by RDP software.
(TIF)

Figure S3 Recombination map of fragment C created by RDP software.
(TIF)

Figure S4 Split phylogenetic trees constructed by MEGA software. clone number and fragment used to construct trees are indicated beside each tree.
(TIF)

Figure S5 Split phylogenetic trees constructed by MEGA software. clone number and fragment used to construct trees are indicated beside each tree.
(TIF)

Figure S6 Split phylogenetic trees constructed by MEGA software. clone number and fragment used to construct trees are indicated beside each tree.
(TIF)

Figure S7 Alignment of fragment A(HBV nt 2813-0-1667)of Y2 clones. Deep green lines are genotype C2, deep pink lines are genotype D1, light green lines are the C2 component of genotype recombinant CD1 and light pink lines are the D1 component of recombinant genotype CD1. The black lines are sequence that is common to the recombining genotypes, and within which the recombination probably occurred. C2 (242): consensus sequence formed by 242 subgenotype C2 sequences from GenBank. D1 (88): consensus sequence formed by 88 subgenotype D1 sequences from GenBank. CD1 (33): consensus sequence formed by CD1 recombinant sequences from GenBank. Y2-1'12: clones from fragment A of Y2 patients.
(DOC)

Figure S8 Alignment of fragment B(HBV nt 1822-0-257) of Y2 clones. Deep green lines are genotype C2, deep pink lines are genotype D1, light green lines are the C2 component of genotype recombinant CD1, light pink lines are the D1 component of recombinant genotype CD1. The black lines are sequence that is common to the recombining genotypes, and within which the recombination probably occurred. C2 (242): consensus sequence formed by 242 subgenotype C2 sequences from GenBank. D1 (88): consensus sequence formed by 88 subgenotype D1 sequences from GenBank. CD1 (33): consensus sequence formed by CD1 recombinant sequences from GenBank. Y2-21'212: clones from fragment B of Y2 patients.
(DOC)

Figure S9 Alignment of fragment C(HBV nt 57-1818) of Y2 clones. Deep green lines are genotype C2, deep pink lines are genotype D1, light green lines are the C2 component of genotype recombinant CD1, light pink lines are the D1 component of recombinant genotype CD1. The black lines are sequence that is common to the recombining genotypes, and within which the recombination probably occurred. C2 (242): consensus sequence formed by 242 subgenotype C2 sequences from GenBank. D1 (88): consensus sequence formed by 88 subgenotype D1 sequences from GenBank. CD1 (33): consensus sequence formed by CD1 recombinant sequences from GenBank. B1B22: clones from fragment C of Y2 patients.
(DOC)

Author Contributions

Conceived and designed the experiments: ZW MM JH. Performed the experiments: BZ ZW. Analyzed the data: BZ JY JS. Contributed reagents/materials/analysis tools: HL YT. Wrote the paper: BZ YT.

References

1. Bilsel PA, Rowe JE, Fitch WM, Nichol ST (1990) Phosphoprotein and nucleocapsid protein evolution of vesicular stomatitis virus New Jersey. J Virol 64: 2498–2504.
2. Okamoto H, Tsuda F, Sakugawa H, Sastrosoewignjo RI, Imai M, et al. (1988) Typing hepatitis B virus by homology in nucleotide sequence: comparison of surface antigen subtypes. J Gen Virol 69 (Pt 10): 2575–2583.
3. Norder H, Hammas B, Lofdahl S, Courouce AM, Magnius LO (1992) Comparison of the amino acid sequences of nine different serotypes of hepatitis B surface antigen and genomic classification of the corresponding hepatitis B virus strains. J Gen Virol 73 (Pt 5): 1201–1208.
4. Gerner PR, Friedt M, Oettinger R, Lausch E, Wirth S (1998) The hepatitis B virus seroconversion to anti-HBe is frequently associated with HBV genotype changes and selection of preS2-defective particles in chronically infected children. Virology 245: 163–172.
5. Liu CJ, Kao JH, Chen DS (2006) Mixed hepatitis B virus genotype infections: the more, the worse? Hepatology 44: 770.
6. Lin CL, Liu CJ, Chen PJ, Lai MY, Chen DS, et al. (2007) High prevalence of occult hepatitis B virus infection in Taiwanese intravenous drug users. J Med Virol 79: 1674–1678.
7. Wang Z, Liu Z, Zeng G, Wen S, Qi Y, et al. (2005) A new intertype recombinant between genotypes C and D of hepatitis B virus identified in China. J Gen Virol 86: 985–990.
8. Zhou B, Xiao L, Wang Z, Chang ET, Chen J, et al. (2011) Geographical and ethnic distribution of the HBV C/D recombinant on the Qinghai-Tibet Plateau. PLoS One 6: e18708.
9. Zeng GB, Wen SJ, Wang ZH, Yan L, Sun J, et al. (2004) A novel hepatitis B virus genotyping system by using restriction fragment length polymorphism patterns of S gene amplicons. World J Gastroenterol 10: 3132–3136.
10. Sugauchi F, Mizokami M, Orito E, Ohno T, Kato H, et al. (2001) A novel variant genotype C of hepatitis B virus identified in isolates from Australian Aborigines: complete genome sequence and phylogenetic relatedness. J Gen Virol 82: 883–892.
11. Gunther S, Li BC, Miska S, Kruger DH, Meisel H, et al. (1995) A novel method for efficient amplification of whole hepatitis B virus genomes permits rapid functional analysis and reveals deletion mutants in immunosuppressed patients. J Virol 69: 5437–5444.
12. Sugauchi F, Orito E, Ichida T, Kato H, Sakugawa H, et al. (2003) Epidemiologic and virologic characteristics of hepatitis B virus genotype B having the recombination with genotype C. Gastroenterology 124: 925–932.
13. Martin D, Rybicki E (2000) RDP: detection of recombination amongst aligned sequences. Bioinformatics 16: 562–563.
14. Heath L, van der Walt E, Varsani A, Martin DP (2006) Recombination patterns in aphthoviruses mirror those found in other picornaviruses. J Virol 80: 11827–11832.
15. Worobey M, Holmes EC (1999) Evolutionary aspects of recombination in RNA viruses. J Gen Virol 80 (Pt 10): 2535–2543.
16. Abdou CM, Brichler S, Mansour W, Le Gal F, Garba A, et al. (2010) A novel hepatitis B virus (HBV) subgenotype D (D8) strain, resulting from recombination between genotypes D and E, is circulating in Niger along with HBV/E strains. J Gen Virol 91: 1609–1620.
17. Phung TB, Alestig E, Nguyen TL, Hannoun C, Lindh M (2010) Genotype X/C recombinant (putative genotype I) of hepatitis B virus is rare in Hanoi, Vietnam–genotypes B4 and C1 predominate. J Med Virol 82: 1327–1333.
18. Fang ZL, Hue S, Sabin CA, Li GJ, Yang JY, et al. (2011) A complex hepatitis B virus (X/C) recombinant is common in Long An county, Guangxi and may have originated in southern China. J Gen Virol 92: 402–411.
19. Mahgoub S, Candotti D, El EM, Allain JP (2011) Hepatitis B virus (HBV) infection and recombination between HBV genotypes D and E in asymptomatic blood donors from Khartoum, Sudan. J Clin Microbiol 49: 298–306.
20. Hannoun C, Norder H, Lindh M (2000) An aberrant genotype revealed in recombinant hepatitis B virus strains from Vietnam. J Gen Virol 81: 2267–2272.
21. Banner LR, Lai MM (1991) Random nature of coronavirus RNA recombination in the absence of selection pressure. Virology 185: 441–445.
22. Kato H, Orito E, Gish RG, Sugauchi F, Suzuki S, et al. (2002) Characteristics of hepatitis B virus isolates of genotype G and their phylogenetic differences from the other six genotypes (A through F). J Virol 76: 6131–6137.

23. Sugiyama M, Tanaka Y, Kato T, Orito E, Ito K, et al. (2006) Influence of hepatitis B virus genotypes on the intra- and extracellular expression of viral DNA and antigens. Hepatology 44: 915–924.
24. Sugiyama M, Tanaka Y, Sakamoto T, Maruyama I, Shimada T, et al. (2007) Early dynamics of hepatitis B virus in chimeric mice carrying human hepatocytes monoinfected or coinfected with genotype G. Hepatology 45: 929–937.
25. Yang J, Xing K, Deng R, Wang J, Wang X (2006) Identification of Hepatitis B virus putative intergenotype recombinants by using fragment typing. J Gen Virol 87: 2203–2215.
26. Tran TT, Trinh TN, Abe K (2008) New complex recombinant genotype of hepatitis B virus identified in Vietnam. J Virol 82: 5657–5663.
27. Simmonds P, Midgley S (2005) Recombination in the genesis and evolution of hepatitis B virus genotypes. J Virol 79: 15467–15476.
28. Morozov V, Pisareva M, Groudinin M (2000) Homologous recombination between different genotypes of hepatitis B virus. Gene 260: 55–65.
29. Owiredu WK, Kramvis A, Kew MC (2001) Hepatitis B virus DNA in serum of healthy black African adults positive for hepatitis B surface antibody alone: possible association with recombination between genotypes A and D. J Med Virol 64: 441–454.
30. Kurbanov F, Tanaka Y, Fujiwara K, Sugauchi F, Mbanya D, et al. (2005) A new subtype (subgenotype) Ac (A3) of hepatitis B virus and recombination between genotypes A and E in Cameroon. J Gen Virol 86: 2047–2056.
31. Tran TT, Trinh TN, Abe K (2008) New complex recombinant genotype of hepatitis B virus identified in Vietnam. J Virol 82: 5657–5663.
32. Tatematsu K, Tanaka Y, Kurbanov F, Sugauchi F, Mano S, et al. (2009) A genetic variant of hepatitis B virus divergent from known human and ape genotypes isolated from a Japanese patient and provisionally assigned to new genotype J. J Virol 83: 10538–10547.
33. Sugauchi F, Orito E, Ichida T, Kato H, Sakugawa H, et al. (2002) Hepatitis B virus of genotype B with or without recombination with genotype C over the precore region plus the core gene. J Virol 76: 5985–5992.

Biomaterials xxx (2012) 1–9

Contents lists available at SciVerse ScienceDirect

Biomaterials

journal homepage: www.elsevier.com/locate/biomaterials

Homo-catiomer integration into PEGylated polyplex micelle from block-catiomer for systemic anti-angiogenic gene therapy for fibrotic pancreatic tumors

Qixian Chen [a], Kensuke Osada [a,**], Takehiko Ishii [b], Makoto Oba [c], Satoshi Uchida [d], Theofilus A. Tockary [a], Taisuke Endo [a], Zhishen Ge [a], Hiroaki Kinoh [a], Mitsunobu R. Kano [e], Keiji Itaka [d], Kazunori Kataoka [a,b,d,*]

[a] Department of Materials Engineering, Graduate School of Engineering, The University of Tokyo, 7-3-1 Hongo, Bunkyo-ku, Tokyo 113-8656, Japan
[b] Department of Bioengineering, Graduate School of Engineering, The University of Tokyo, 7-3-1 Hongo, Bunkyo-ku, Tokyo 113-0033, Japan
[c] Department of Clinical Vascular Regeneration, Graduate School of Medicine, The University of Tokyo, 7-3-1 Hongo, Bunkyo-ku, Tokyo 113-8655, Japan
[d] Division of Clinical Biotechnology, Center for Disease Biology and Integrative Medicine, Graduate School of Medicine, The University of Tokyo, 7-3-1 Hongo, Bunkyo-ku, Tokyo 113-0033, Japan
[e] Department of Molecular Pathology, Graduate School of Medicine, The University of Tokyo, 7-3-1 Hongo, Bunkyo-ku, Tokyo 113-8655, Japan

ARTICLE INFO

Article history:
Received 9 February 2012
Accepted 4 March 2012
Available online xxx

Keywords:
DNA
Micelle
Nanoparticle
Gene transfer
In vitro test
In vivo test

ABSTRACT

Homo-poly{*N'*-[*N*-(2-aminoethyl)-2-aminoehtyl]aspartamide} [PAsp(DET), **H**] was attempted to integrate into poly (ethylene glycol) (PEG)-*b*-PAsp(DET)] (**B**) formulated polyplex micelle with the aim of enhancing cell transfection efficiency for PEGylated polyplex micelle via **H** integration. *In vitro* evaluations verified **H** integration of potent stimulation in enhancing cell-transfecting activity of PEGylated polyplex micelles via promoted cellular uptake and facilitated endosome escape. *In vivo* anti-angiogenic tumor suppression evaluations validated the feasibility of **H** integration in promoting gene transfection to the affected cells via systemic administration, where loaded anti-angiogenic gene remarkably expressed in the tumor site, thereby imparting significant inhibitory effect on the growth of vascular endothelial cells, ultimately leading to potent tumor growth suppression. These results demonstrated potency of **H** integration for enhanced transfection activity and potential usage in systemic applications, which could have important implications on the strategic use of **H** integration in the non-viral gene carrier design.

1. Introduction

In recent years, development of non-viral gene delivery carriers has been highlighted with respect to their advantages in low host immunogenicity and large-scale manufacturing [1,2]. Cationic gene carriers, which are formulated through electrostatic self-assembly of anionic plasmid DNA (pDNA) and cationic materials (e.g. polycations, cationic lipids), have emerged as a tempting gene delivery modality in view of their tremendous potential to circumvent ensemble of predefined biological barriers via engineering their chemistry [3]. The principle design criteria in view of the barriers encountered in delivery of exogenous gene to the targeted cells include the abilities of protecting encapsulated pDNA from enzymatic degradation, preventing undesired non-specific interactions in the biological environment, readily being internalized into the affected cells and retrieving from endosome entrapment [4]. To these required principles, we have developed a multifunctional catiomer, poly{*N'*-[*N*-(2-aminoethyl)-2-aminoehtyl] aspartamide} PAsp (DET) (**H**) [5–8]. This PAsp(DET) catiomer featured as the flanking ethylenediamine moiety in the side chain of N-substituted polyaspartamide (PAsp), displayed distinctive two-step protonation behavior in response to pH gradient, where the protonation of ethylenediamine is facilitated in acidic pH. Interestingly, this acid-responsive trait of PAsp(DET) elicits a selective endosome membrane destabilization function. In contrast to minimal membrane destabilization at physiological pH, fully protonated PAsp(DET) in acidic endosome milieu exerts strikingly explosive destabilization power on cellular membrane, accordingly results in liberation of embedded gene from endosome entrapment to the cytosol and efficient gene transfection without penalty in cell viability [6,9,10]. Still, PAsp(DET) that remains in the cytosol will not provoke cumulative cytotoxic concern due to its appreciable self-catalytic degradable nature, consequently allowing safe gene expression in the affected cells [7].

* Corresponding author. Department of Materials Engineering, Graduate School of Engineering, The University of Tokyo, 7-3-1 Hongo, Bunkyo-ku, Tokyo 113-0033, Japan. Tel.: +81 3 5841 7138; fax: +81 3 5841 7139.
** Corresponding author. Tel.: +81 3 5841 1654; fax: +81 3 5841 7139.
E-mail addresses: osada@bmw.t.u-tokyo.ac.jp (K. Osada), kataoka@bmw.t.u-tokyo.ac.jp (K. Kataoka).

0142-9612/$ – see front matter © 2012 Elsevier Ltd. All rights reserved.
doi:10.1016/j.biomaterials.2012.03.017

Please cite this article in press as: Chen Q, et al., Homo-catiomer integration into PEGylated polyplex micelle from block-catiomer for systemic anti-angiogenic gene therapy for fibrotic pancreatic tumors, Biomaterials (2012), doi:10.1016/j.biomaterials.2012.03.017

On the other hand, it is well acknowledged that direct use of homo-catiomer formulations in systemic therapy was limited since they can readily interact with charged components in the blood stream, in consequence subjected to rapidly clearance by reticulo-endothelial system or macrophage cells. To improve the biocompatibility and bioavailability of **H** formulation, surface modification of polyion complex with poly(ethylene glycol) (PEG) was developed via complexation of block-catiomer PEG-*b*-PAsp(DET) (**B**) with pDNA, where single pDNA can be packaged into nanosized core covered by the hydrophilic and biocompatible PEG corona [5]. With merits of this PEG shielding shell, non-specific interactions with biological components were minimized and allows for well dispersing in the blood fluid to stealthily circulate [11]. However, PEG shell reduces affinity to cell membrane so that transfection efficiency extends significance for the ultimate therapeutic potency. In light of dramatic high cell-transfecting activity mediated by homo-PAsp(DET) (**H**) compared to **B** [12], we are encouraged to integrate **H** into **B** based polyplex micelle in pursuit of enhancement for the cell transfection efficiency of PEGylated polyplex micelle in virtue of **H** integration and ultimately achieving improved drug efficacy at the targeted site via systemic administration. Indeed, our recent study has validated feasibility of such block copolymer and homo polymer combined polyplex micelles (**BHPMs**) with pronounced enhancement in transfection efficiency via intratracheal lung administration and remarkably reduced inflammatory response due to inactivated macrophage recognition to polyplexes with PEG shielding [13].

In the present work, we studied the functionalities of **H** integration to PEGylated polyplex micelle and identified the most appreciable combinatorial ratio of **B** and **H** for systemic application. The identified **BHPM** containing anti-angiogenic gene was utilized for treatment of pancreatic tumor bearing mice to demonstrate the utility of **BHPM** for systemic anti-angiogenic tumor therapy.

2. Materials and methods

2.1. Materials

α-Methoxy-ω-amino-poly(ethylene glycol) (M_w 12,000) was obtained from Nippon Oil and Fats Co., Ltd. (Tokyo, Japan). β-Benzyl-L-aspartate N-carboxyanhydride (BLA-NCA) was obtained from Chuo Kaseihin Co., Inc. (Tokyo, Japan). Diethylenetriamine (DET), N,N-dimethylformamide (DMF), n-butylamine, dichloromethane, benzene, and trifluoroacetic acid were purchased from Wako Pure Chemical Industries, Ltd. Alexa-488 succinimidyl ester was a product of Invitrogen (Carlsbad, CA). Fetal bovine serum (FBS) was purchased from Dainippon Sumitomo Parma Co., Ltd. (Osaka, Japan). The pDNAs, pBR322 (4,363 bp) and pGL3 control vector (5,256 bp) were purchased from Takara Bio Inc. (Otsu, Japan). The pDNA encoding luciferase with a CAG promoter provided by RIKEN Gene Bank (Tsukuba, Japan) was amplified in competent DH5α *Escherichia coli* and purified with a QIAGEN HiSpeed Plasmid MaxiKit (Germantown, MD). Cell culture lysis buffer and luciferase Assay System Kit was purchased from Promega Co. (Madison, WI). The Micro BCA™ Protein Assay Reagent Kit was purchased from Pierce Co., Inc. (Rockford, IL). The pDNA encoding a soluble form of VEGF receptor-1 (sFlt-1) was a kind gift from Prof. Masabumi Shibuya in Tokyo Medical and Dental University, and was prepared as previously reported [14]. Dulbecco's modified Eagle's medium (DMEM) was purchased from Sigma–Aldrich (St. Louis, MO). For cellular uptake and intracellular distribution assay, pDNA was labeled with Cy5 using a Label IT Nucleic Acid Labeling Kit from Mirus Bio Corporation (Madison, WI) according to the manufacturer's protocol. Human hepatoma cells (HuH-7) and human umbilical vein endothelial cells (HUVEC) were obtained from the Japanese Collection of Research Bioresources Cell Bank (Tokyo, Japan) and Lonza Ltd. (Basel, Switzerland), respectively. BALB/c nude mice (female, 5 weeks old) were purchased from Charles River Laboratories (Tokyo, Japan). All animal experimental protocols were established according to the guidelines of the Animal Committee of the University of Tokyo.

2.2. Synthesis of *B* and *H*

B and **H** were prepared according to a ring-opening polymerization scheme as previously reported [5,7]. In brief, the polymerization of monomer BLA-NCA was initiated from the ω-NH_2 terminal group of α-methoxy-ω-amino-poly (ethylene glycol) (M_w 12,000) (for block-catiomer, **B**) or *n*-butylamine (for homo-catiomer, **H**) to obtain PEG-PBLA or PBLA, respectively, followed by aminolysis reaction to introduce diethylenetriamine molecules into the side chain of PBLA. The prepared polymers were determined to have a narrow unimodal molecular weight distribution (**B**: $M_w/M_n = 1.05$; **H**: $M_w/M_n = 1.06$) by gel permeation chromatography. The polymerization degree of PAsp(DET) segment in **B** was confirmed to be 61 from the peak intensity ratio of the methylene protons in PEG (-OCH_2CH_2-, $\delta = 3.7$ ppm) to the methylene groups in the bis-ethylamine of PAsp(DET): $NH_2(CH_2)_2NH(CH_2)_2NH$-$\delta = 3.1–3.5$ ppm settled in the side chain in the ^{1}H NMR spectrum in D_2O at 25 °C. The polymerization degree of **H** was confirmed to be 55 according to the peak intensity ratio of the protons of the butyl group at the α-chain end CH_3- to the methylene groups in the bis-ethylamine of PAsp(DET) in the ^{1}H NMR spectrum in D_2O at 25 °C.

2.3. Preparation of *BHPMs*

Synthesized **B** and **H** powders were separately dissolved in 10 mM HEPES buffer (pH 7.4) as stock solution. Mixture of **B** and **H** stock solutions at varying **B/H** ratios (residual molar ratio of amino groups in **B** and **H**) was added to pDNA solution for complexation at varying N/P ratios (residual molar ratio of total amino groups in **B** and **H** to phosphate groups in pDNA), followed by overnight incubation at 4 °C. The final concentration of pDNA in all the samples was adjusted to 33.3 μg/mL. Note that all the pre-experimental procedures involved with polymer solution or complex solution were strictly carried out at low temperature, e.g. 4 °C refrigerator or ice bath to avoid polymer degradation [7]. Polyplex micelle formulated from **B** and pDNA was referred hereafter as **B100**, and polyplex formulated from **H** and pDNA was referred hereafter as **H100**.

2.4. Dynamic light scattering

The size and polydispersity index (PDI) of **BHPMs** were determined from the dynamic light scattering (DLS) measurement by the Zetasizer nanoseries (Malvern Instruments Ltd., UK) at a detection angle of 173° and a temperature of 25 °C. **BHPMs** were prepared as described above for three times measurement. The data derived from the rate of decay in the photon correlation function were treated from a cumulant method, and the corresponding diameter of each sample was calculated according to the Stokes–Einstein equation [15].

2.5. Zeta potential

The zeta potential of **BHPMs** was determined from the laser-doppler electrophoresis using the Zetasizer nanoseries (Malvern Instruments Ltd., UK). According to the obtained electrophoretic mobility, the zeta potential of each sample ($n = 3$) was calculated according to the Smoluchowski equation: $\zeta = 4\pi\eta\nu/e$, where η is the viscosity of the solvent, ν is the electrophoretic mobility, and e is the dielectric constant of the solvent.

2.6. Transmission electron microscopy (TEM) measurement

TEM observation was conducted using an H-7000 electron microscope (Hitachi, Tokyo, Japan) operated at 75 kV acceleration voltages for insight on the morphology of **BHPMs** containing pBR322 pDNA. Copper TEM grids with carbon-coated collodion film were glow-discharged for 10 s using an Eiko IB-3 ion coater (Eiko Engineering Co. Ltd., Japan). The grids were dipped into desired **BHPM** solution, which was pre-mixed with uranyl acetate solution (2% (w/v)), for 30 s. The sample grids were blotted by filter paper to remove excess complex solution, followed by air-drying for 30 min. The morphology of the prepared **BHPMs** was determined from the TEM images obtained by staining pDNA with uranyl acetate (UA). Note that PEG shell is invisible under TEM due to its low affinity with UA. Thus, the contours of pDNA strands in the complex were selectively visualized without interference from PEG moieties surrounding pDNA strands. The obtained TEM image was further analyzed by Image J 1.44 (National Institutes of Health) to quantify the length of major axis in each sample, and 100 individual nanoparticles were measured for distribution.

2.7. Binding numbers of *B* and *H* to pDNA in *BHPMs*

The binding behaviors of **B** and **H** to pDNA in each **BHPM** were investigated according to a preparative ultracentrifuge method. As reported previously [14], ultracentrifugation of complex solution allows selective sedimentation of polyplex micelles, while unbound free polymers remain in the supernatant. In consequence, the binding fraction of polymer can be determined by subtracting free polymer (remain in the supernatant after sedimentation) from the total fed polymer. For instance, to quantify the associating number of **B** in the **BHPMs**, Alexa-488 labeled **B** (labeling procedures according to protocol provided by the manufacture, conjugation efficiency: 0.41 Alexa-488 molecules per **B**) and non-labeled **H** were used to prepare a class of **BHPMs** at varying **B/H** ratio, N/P 8 with pDNA (pGL3 control vector). After overnight incubation at 4 °C, 500 μL aliquot of each **BHPM** solution was injected into thickwall polycarbonate tube, 343776 (Beckman Coulter, Inc., Fullerton, CA) and subjected to ultracentrifugation (Optima TLX, Beckman Coulter, Inc., Fullerton, CA) equipped with TLA-120.1 rotor for 3 h under 50,000 *g* for complete

Please cite this article in press as: Chen Q, et al., Homo-catiomer integration into PEGylated polyplex micelle from block-catiomer for systemic anti-angiogenic gene therapy for fibrotic pancreatic tumors, Biomaterials (2012), doi:10.1016/j.biomaterials.2012.03.017

sedimentation of **BHPMs**. The supernatant with the content of free **B** was collected for fluorescence intensity measurement using a spectrofluorometer (ND-3300, NanoDrop, Wilmington) with an excitation wavelength of 470 nm and an emission wavelength of 519 nm. The concentration of free **B** in the supernatant or the fed **B** solution prior to ultracentrifugation was determined from the obtained fluorescence intensity according to a calibration curve from Alexa488-labeled **B** solutions. Same method was applied to determine the binding number of **H** (conjugation efficiency: 0.34 Alexa-488 molecules per **H**) to pDNA.

2.8. In vitro transfection efficiency

HuH-7 cells were seeded on 24-well culture plates (20,000 cells/well) and incubated overnight in 400 μL of DMEM containing 10% FBS in a humidified atmosphere with 5% CO_2 at 37 °C. The medium was replaced with 400 μL of fresh medium, followed by addition of 30 μL each **BHPM** solution (prepared at N/P 8, 1 μg pDNA/well). After 24 h incubation, the medium was exchanged with 400 μL fresh DMEM, followed by another 24 h incubation. The cells were washed with 400 μL of PBS, and lysed in 150 μL of the cell culture lysis buffer. The luciferase activity of the lysates was evaluated from the photoluminescence intensity using Mithras LB 940 (Berthold Technologies, USA). The obtained luciferase activity was normalized according to corresponding amount of proteins in the lysates determined by the Micro BCATM Protein Assay Reagent Kit.

2.9. Cellular uptake

Cellular uptake efficiency was evaluated by flow cytometry (BD LSR II, BD, Franklin Lakes, NJ). Cy5-labeled pDNA were used to prepare a group of **BHPMs**. HuH-7 cells were seeded on 6-well culture plate (100,000 cells/well) and incubated overnight in 2 mL of DMEM containing 10% FBS. The medium was replaced with fresh medium, followed by addition of 150 μL **BHPM** solution (33.3 μg pDNA/mL) into each well. After 24 h incubation, the cells were washed 3 times with PBS to remove extracellular Cy5 fluorescence. After detachment by trypsin from the culture plate, the cells were harvested and re-suspended in PBS for flow cytometry measurement.

2.10. Intracellular distribution

Endosome escape capacity was determined by evaluating colocalization degree of pDNA and endosome by Confocal laser scanning microscopy (CLSM). In brief, Cy5-labeled pDNA were used to prepare a class of **BHPMs** at N/P 8. HuH-7 cells (50,000 cells) were seeded on 35 mm cell culture dishes and incubated overnight in 1 mL of DMEM containing 10% FBS. The medium was replaced with fresh medium, followed by addition of 75 μL **BHPM** solution (33.3 μg pDNA/mL) into each cell culture dishes. After 24 h incubation, the medium was removed and the cells were rinsed three times with PBS prior to the imaging. The intracellular distribution of each **BHPM** was observed by CLSM after staining acidic late endosomes and lysosomes with LysoTracker Green (Molecular Probes, Eugene, OR) and nuclei with Hoechst 33342 (Dojindo Laboratories, Kumamoto, Japan). The CLSM observation was performed using LSM 510 (Carl Zeiss, Germany) with a 63 × objective (C-Apochromat, Carl Zeiss, Germany) at excitation wavelengths of 488 nm (Ar laser), 633 nm (He-Ne laser), and 710 nm (MaiTai laser for 2-photon imaging) for LysoTrakcer Green (green), Cy5 (red), and Hoechst 33342 (blue), respectively. The colocalization ratio was calculated as previously described [9,12,14] according to the formula:

Colocalization ratio = number of yellow pixels/number of yellow and red pixels,

where yellow corresponds to the pDNA that is trapped into endosome, while red corresponds to the pDNA that is released into the cytosol.

2.11. Release of *H* in endosome milieu

A group of **BHPMs** containing pGL3 control vector was prepared with Alexa488-labeled **H** at varying **B/H** ratio, N/P 2 (approximate stoichiometric charge ratio) in 10 mM HEPES buffer (pH 7.4). After overnight incubation at 4 °C, aliquot of each **BHPM** solution was mounted by 50 mM acetic acid/acetic sodium buffer (the final pH was adjusted to be 5 for mimicking endosome milieu), followed by another 48 h incubation at 4 °C. The released number of **H** from each **BHPM** was quantified by preceding ultracentrifuge measurement. The releasing percentage was calculated according to the formula:

Released **H** (%) = $(\mathbf{H}_{7.4} - \mathbf{H}_5)/\mathbf{H}_{7.4} \times 100$ (%)

where $\mathbf{H}_{7.4}$ denotes associating number of **H** on a pDNA at pH 7.4, and $\mathbf{H}_5$ denotes associating number of **H** on a pDNA after 48 h incubation of **BHPMs** at pH 5.

2.12. Cell viability

HuH-7 cells or HUVEC were seeded in 24-well culture plates (20,000 cells/well) and incubated overnight in 400 μL DMEM supplemented with 10% FBS (or MCDB131 containing 10% FBS and 10 ng/mL b-FGF for HUVEC). The medium was replaced with 400 μL of fresh medium, followed by addition of 30 μL each **BHPM** solution into each well (1 μg pDNA/well). After 24 h incubation at 37 °C, the medium was changed to 400 μL of fresh medium, followed by another 24 h incubation. The cells were washed with 400 μL, and cell viability was determined using the Cell Counting Kit-8 (Dojindo, Kumamoto, Japan) according to the manufacturer's protocol. Each well in 200 μL fresh medium was reacted with 20 μL Cell Counting Kit-8 Agent. After 2 h reaction at 37 °C, the absorbance at 450 nm of the formazan in each well was quantified from a microplate reader (Model 680, Bio-rad, UK). The cell viability in each well was calculated and presented as a percentage of control wells without any addition.

2.13. Tumor suppression efficacy

BALB/c nude mice were inoculated subcutaneously with BxPC3 cells (5×10^6 cells in 100 μL of PBS). Tumors were allowed to grow for 3 weeks till proliferative phase (the size of the tumors was approximately 50 mm^3). Subsequently, each sample (20 μg sFlt-1 pDNA/mouse) in 10 mM HEPES buffer (pH 7.4) with 150 mM NaCl was intravenously injected via the tail vein 3 times on days 0, 4 and 8. Tumor size was measured every two or three days by a digital vernier caliper across its longest (a) and shortest diameters (b), and its volume (V) was calculated according to the formula $V = 0.5\ ab^2$. Tumor progression was evaluated in terms of relative tumor volume (to day 0) over a period of 28 days, $n = 6$.

2.14. Vascular density

BHPMs loading either sFlt-1 or Luc pDNA (20 μg of pDNA) were intravenously injected into the BxPC3-inoculated mice though the tail vein on days 0 and 4. Mice were sacrificed on day 6, and the tumors were excised, frozen in dry-iced acetone, and sectioned into 10 μm thick slices with a cryostat. Vascular endothelial cells (VECs) were immunostained by rat monoclonal antibody antiplatelet endothelial cell adhesion molecule-1 (PECAM-1) (BD Pharmingen, Franklin Lakes, NJ), followed by incubation with Alexa Fluor 488-conjugated secondary antibody. The immunostained sections were observed with CLSM (Carl Zeiss, Germany). The vascular density was quantified by counting the percentage area of PECAM-1-positive pixels per image with 15 images per sample.

2.15. sFlt-1 expression in the tumor site

BHPMs loading sFlt-1 (20 μg of pDNA) were intravenously injected into the BxPC3-inoculated mice via the tail vein. Mice were sacrificed at 48 h after injection. The tumors were excised, frozen in dry-iced acetone, and sectioned into 10 μm thick slices with a cryostat. VECs were immunostained using antibodies anti-mouse PECAM-1 (BD Pharmingen, USA) and anti-human and mouse VEGFR1 (ab32152, Abcam Japan, Tokyo, Japan). The sections immunostained was observed with CLSM (Carl Zeiss, Germany). The sFlt-1 gene expression was quantified by counting the percentage area of ab32152-positive pixels per image with 6 images per sample.

3. Results and discussion

3.1. Characterizations of *BHPMs*

One of most important factors for developing gene delivery carriers is possession of nanosized dimensions and stealth surface characteristics to enable circulation in the blood stream to the targeted tissue. In this respect, the size and zeta potential of **BHPMs** were examined. From the size characterization by DLS, all **B**-included samples presented cumulant diameters ranging from 60 nm to 100 nm (Supplementary Table S1) with unimodal size distributions of low PDI from 0.1 to 0.2 (Supplementary Table S2), whereas **H100** presented remarkably larger size over 1000 nm at a critical N/P range of 1.5–2. In the range over this critical N/P range ($N/P \geq 2$), **H100** possessed comparable size of approximate 75 nm with unimodal size distribution.

The zeta potential of **BHPMs** was examined because possession of neutral zeta potential is necessary to diminish non-specific interactions with biological components, protein adsorption, aggression, opsonization [16,17]. For this purpose, the zeta potential of **BHPMs** was examined. Overall, negative net charge of pDNA in all complexes was approximately neutralized at a critical N/P of 1.5–2, which is consistent with the protonation degree (53%) of amino groups in PAsp(DET) at neutral pH 7.4 [5]. This suggests aforementioned large-sized formulation of **H100** at this critical N/P range may form through the secondary aggregation of the charge neutralized polyplexes. In the range above this critical N/P range, **H100** ($N/P \geq 2$) possessed remarkable positive value in zeta potential approximate +40 mV (Supplementary Table 3). On the

Please cite this article in press as: Chen Q, et al., Homo-catiomer integration into PEGylated polyplex micelle from block-catiomer for systemic anti-angiogenic gene therapy for fibrotic pancreatic tumors, Biomaterials (2012), doi:10.1016/j.biomaterials.2012.03.017

contrary, the zeta potential of **B100** was significantly suppressed to neutral approximate +5–6 mV, indicating charge-masking effect of PEGylation from **B**. To our interests, the neutral zeta potential remained for the **BHPMs** with **H**% ≤ 50%, though **BHPM** at **B**/**H** = 75/25 showed higher zeta potential (over +10 mV) possibly ascribe to insufficient PEG shielding due to low **B** content. Each group of **BHPMs** with same **H**% (over than stoichiometric charge ratio, N/P ≥ 2) showed comparable size and zeta potential regardless of N/P ratios. Here, we choose **BHPMs** prepared at N/P 8 as representative for hereafter investigations.

The morphology of **BHPMs** was investigated by TEM measurement (Fig. 1). Note that pDNA strands in the **BHPMs** were selectively observed in the TEM image due to stronger affinity of uranyl acetate (UA) to DNA compared to PEG. **B100** presents as uniform rod-shaped particles (Fig. 1a), suggesting DNA strand is packaged into the rod-shaped bundle through a regular folding behavior [18]. In contrast, **H100** in absence of PEG surface tethering adopted a completely collapsed spherical configuration (Fig. 1d). This stark contrast implied the crucial role of the tethered PEG chains in mediating pDNA packaging. To obtain this collapsed spherical configuration using **B**, the tethered PEG chains must be stuffed as a corona surrounding the spherical core. Apparently, this PEG crowding hinders segmental motion of PEG chains, which is unfavorable with respect to conformational entropy. Hence, it is reasonable to assume that osmotic pressure caused by the crowded PEG chains sustains pDNA collapsing induced by PAsp(DET) binding. Presumably, the tethered PEG may regulate pDNA packaging configurations. According to this discipline, an intermediate pDNA packaging configuration may reside in **BHPMs** by reducing tethered PEG chains. The TEM observations approved our speculations and revealed progressive pDNA configuration change from rod to ellipsoid with shortened length of major axis (58 nm - 44 nm, Fig. 1e) in **BHPMs** along a decreasing content of **B** (Fig. 1b and c) and ultimately collapsed into spherical configuration in the absence of **B** (**H100**). This tendency coincides with the prior DLS measurement, where smaller size and lower PDI were obtained at lower **B**%. Of note, this **B**/**H** ratio dependent manner in pDNA packaging configuration implies the binding content of **B** and **H** to pDNA relies on the fed **B**/**H** ratios.

To gain direct insight on the binding fashions of **B** and **H** to pDNA, the compositions of **B** and **H** in **BHPMs** were quantified according to ultracentrifuge technique. In principle, appropriate ultracentrifugal field was applied for selective sedimentation of complexes, whereas unbound polymer to pDNA (free polymer) stays in the solution. Appending fluorescence dye to **B** (vice versa for **H**), the binding compositions of **B** can be quantified by comparing the total fed number of **B** and the free number of **B**. Overall, the binding compositions of **B** and **H** in the **BHPMs** remain fairly consistent with the fed **B**/**H** ratios (Fig. 2a). Interestingly, identical number of amino groups was found for complexation with one pDNA. Since the bound PAsp(DET)s onto a pDNA possessed 20,000 amino groups in total, in which 53% of amino groups (10,600) presumes to be positively charged at pH 7.4, which coincide with the number of phosphate groups in one pDNA (pGL3: 10,652 negative charges from 5,326 bps). All the **BHPMs** appeared to be formulated exclusively according to stoichiometric charge ratio independent on the fed **B**/**H** ratio. This result provides essential insight on **BHPMs** formulation with the binding ratio of **B** and **H** according to the fed **B**/**H** ratio, thereby allowing precise control of compositions in **BHPMs** by simply altering the fed **B**/**H** ratios.

In summary, we have successfully integrated **H** into polyplex micelle and fabricated distinct PEGylated **BHPM** micelle formulation with neutral zeta potential in the range of **H** ≤ 50%. In addition, the composition of **B** and **H** in **BHPMs** can be facile controlled by varying fed **B** and **H** ratio. The biological impacts of **H** integration on PEGylated polyplex micelle were then investigated.

3.2. Enhanced cellular transfection of *BHPMs* from *H* integration

The transfection efficiency of **BHPMs** was evaluated to verify the effect of **H** integration. Notably, **H** integration appeared to significantly enhance transfection efficiency of polyplex micelle, whereas no observable transfection activities were found in **B100** (Fig. 3). In particular, a pronounced jump of transfection efficiency was observed from the point of **H**% of 30%, e.g. **BHPM** at **B**/**H** = 50/50 capable of mediating comparable high level of transfection efficiency as **H100**. This result approved the powerful potency of **H** integration in enhancing transfection activity of PEGylated polyplex micelle. To understand how **H** integration to PEGylated polyplex micelle worked in transfection, we examined cellular uptake efficiency and endosome escape capacity of **BHPMs** as varying **H**

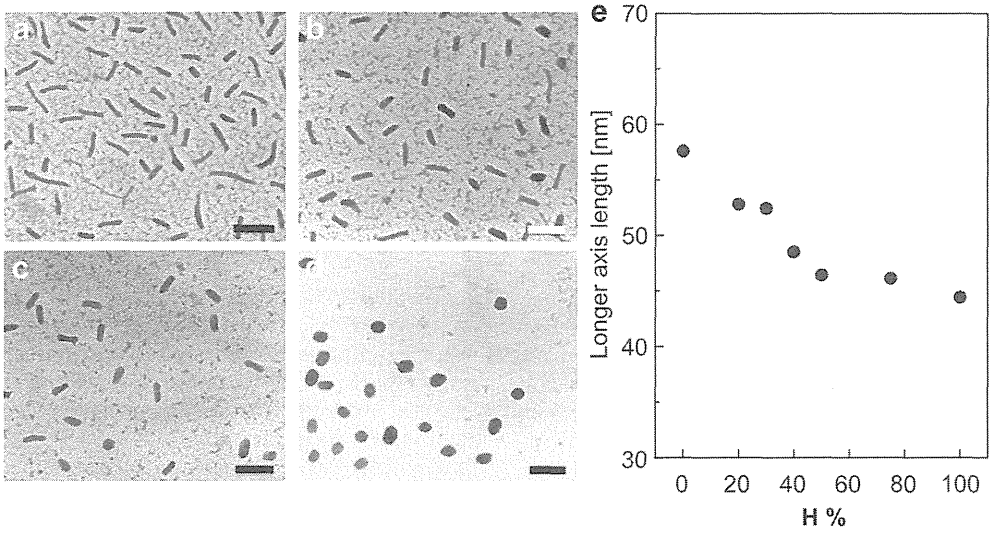

Fig. 1. Morphology of **BHPMs** at varying **H** integration ratio according to TEM observation. a)–d): Representative TEM images of **BHPMs** at varying **H** integration ratio, a) **B**/**H** = 100/0; b) **B**/**H** = 70/30; c) **B**/**H** = 50/50; and d) **B**/**H** = 0/100. The scale bars represent 100 nm in all TEM images. e) Number average length of major axis of **BHPMs** at varying **H** integration ratio analyzed according to acquired TEM images (n = 100).

Please cite this article in press as: Chen Q, et al., Homo-catiomer integration into PEGylated polyplex micelle from block-catiomer for systemic anti-angiogenic gene therapy for fibrotic pancreatic tumors, Biomaterials (2012), doi:10.1016/j.biomaterials.2012.03.017

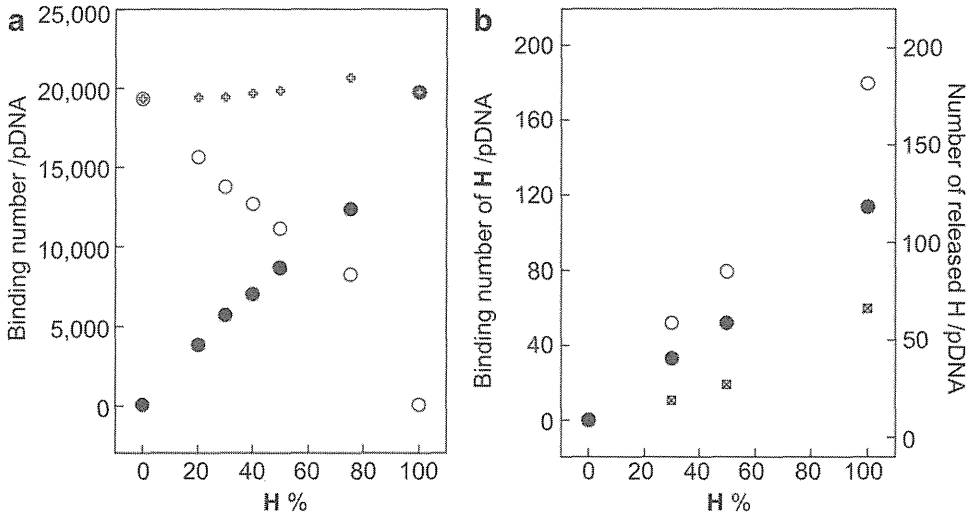

Fig. 2. Binding fashions of **B** and **H** to pDNA in **BHPMs** at varying **H** integration ratio. a): Binding compositions of **B** and **H** in **BHPMs** at pH 7.4. Open circles: **B**; Closed circles: **H**; Open crosses: **B** + **H**. Binding quantity of **B** or **H** in **BHPMs** was expressed as the number of amino groups from associated **B** or **H** per pGL3 pDNA. b): Binding number of **H** chains per pGL3 pDNA at pH 7.4 or pH 5. Open circles: pH = 7.4; Closed circles: pH = 5. Crossed squares: released number of **H** was calculated from comparison of binding numbers of **H** at pH 7.4 and pH 5.

integration ratio because these two events are the crucial factors determining the magnitude of transfection efficiency. The cellular uptake efficiency of **BHPMs** was evaluated by quantifying the internalized pDNA using flow cytometry analysis (Fig. 4a). In consistent with the transfection tendency, no observable cellular uptake was found in **B100**, whereas **BHPMs** exhibited striking contrast with remarkable enhancement in cellular uptake efficiency, e.g. **BHPMs** at **B/H** = 70/30 and 50/50 experienced potent promotion in cellular uptake activity (comparable to **H100**). The

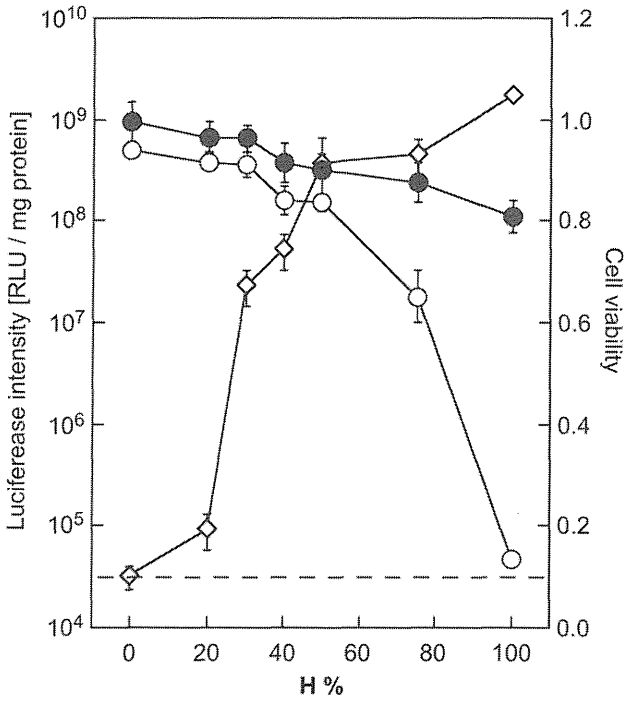

Fig. 3. Transfection efficiency and cell viability of **BHPMs** at varying **H** integration ratio. Dotted line: background level of transfection efficiency in HuH-7. Open diamonds: transfection efficiency of **BHPMs** in HuH-7 cells; Closed circles: cell viability of HuH-7 cells; Open circles: cell viability of HUVEC cells (mean ± SEM, n = 4).

results suggest powerful potency of **H** integration in promoting cellular uptake of PEGylated polyplex micelle. Possibly, decrease of PEG chains in the **BHPMs** with increasing **H** content may facilitate cellular uptake because PEGylation reduces affinity of PEGylated nanocarriers to cell adhesion [19,20]. The detailed underlying mechanism for this enhancement in cellular uptake is ongoing.

The internalized **BHPMs** after endocytosis are subjected to endosome entrapment and eventually end up with enzymatic degradation if they cannot afford adequate facilities to retrieve the entrapped gene from late endosome [21]. Hence, intracellular distributions of **BHPMs** were characterized by CLSM observations (Fig. 4). No significant amount of pDNA (stained as red) localized inside the cells for **B100** (Fig. 4b), which is in agreement with flow cytometry result. On the contrary, **BHPMs** at **B/H** = 70/30 and 50/50 and **H100** (Fig. 4c–e) reveals larger amount of pDNA were internalized into the cells than **B100**. Endosome escape capacities of **BHPMs** were studied in term of quantifying colocalization degrees of pDNA and late-endosome/lysosome (green), thus lower colocalization degree represented higher endosome escape capacity. Interestingly, colocalization ratios of **BHPMs** appeared to follow a clear **H** content dependent manner (Fig. 4a), where lower colocalization ratio attained in the **BHPMs** with larger **H** content. This tendency suggests **H** integration played a prominent role in mediating the release of **BHPMs** from endosome entrapment. A plausible reason for this tendency may lean on the potent membrane disrupting activity of **H** in endosome milieu [6]. As we demonstrated previously, the membrane destabilizing capacity of **H** was low at pH 7.4, while it was remarkably high in acidic condition (endosome milieu), which gave rise to substantially enhanced potency of **H** in endosome escape. In light of the fact that **BHPMs** were self-assembled according to stoichiometric charge ratio, it is reasonable to anticipate that some fraction of integrated **H** might be released from **BHPMs** in endosome milieu, which accounts for endosome membrane disruption. At physiological milieu (pH = 7.4), the ethylenediamine side chain of PAsp(DET) takes almost monoprotonated form with the protonation degree of 0.53, while the protonation was facilitated by acidification, e.g. the majority of ethylenediamine side chain takes double protonated form in endosome milieu with the protonation degree of 0.90 (pH = 5) [6]. The promoted protonation of PAsp(DET) would

Please cite this article in press as: Chen Q, et al., Homo-catiomer integration into PEGylated polyplex micelle from block-catiomer for systemic anti-angiogenic gene therapy for fibrotic pancreatic tumors, Biomaterials (2012), doi:10.1016/j.biomaterials.2012.03.017

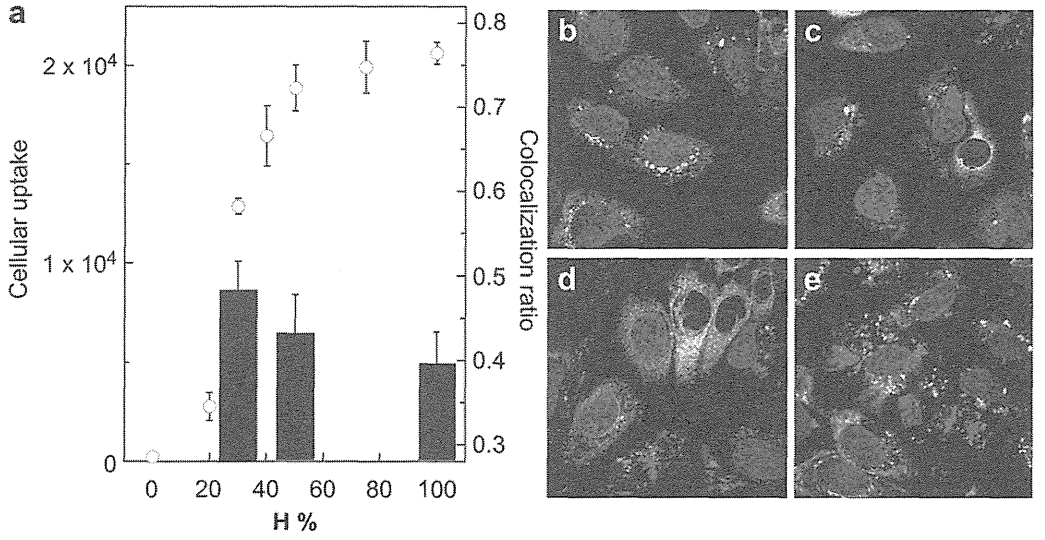

Fig. 4. Cellular uptake and endosome escape profiles of **BHPMs** at varying **H** integration ratio. Open circles: Cellular uptake efficiency of **BHPMs** to HuH-7 cells (mean ± SEM, $n = 3$). b) - e): CLSM images for insight on intracellular distributions of **BHPMs** at varying **H** integration ratio. b) **B/H** = 100/0; c) **B/H** = 70/30; d) **B/H** = 50/50; and e) **B/H** = 0/100. Blue: nucleus; Green: late endosome or lysosome; Red: pDNA. Endosome escape was determined by quantifying colocalization ratio of pDNA and late-endosome/lysosome as summarized in (a) as bar graph (mean ± SEM, $n = 10$). The scale bars represent 10 μm in all CLSM images. (For interpretation of the references to color in this figure legend, the reader is referred to the web version of this article.)

concomitantly elicit transient over-stoichiometric charge for the polyion complex core. Apparently, this transient over-stoichiometric complex are not stable due to the electrostatic repulsion of excessive charged cationers in the complex and would readily release charged chains in the polyion complex to recover electrostatic equilibrium. For evidence of this speculation, a class of **BHPMs** prepared in the HEPES buffer (pH 7.4) was subjected for pH 5 for mimicking endosome entrapment. The remaining binding numbers of **H** per pDNA in **BHPM** were quantified by ultracentrifuge analysis as aforementioned and compared to original binding numbers of **H** per pDNA at pH 7.4. Fig. 2b approves considerable amount of integrated **H** released from each **BHPM** at pH 5 as compared to that at pH 7.4. The releasing numbers of **H** displayed a clear **H** integration ratio dependent manner, where those **BHPMs** with higher **H**% tend to release more. Accordingly, we may speculate that the releasing fraction of **H** would exert disruption of endosome membrane so that allowing for facilitated endosome escape. Indeed, our recent study has verified **H** of powerful membrane destabilization potency in acidic endosome milieu [13], thus approved **H** integration as a convincing strategy in facilitating pDNA release from endosome entrapment.

Minimizing the cytotoxicity, aside from increasing efficacy, is one of key factors in establishing safer gene carriers which are clinically applicable. In this respect, we assessed cell viability in presence of **BHPMs** for two cell lines. First, cell viability was accessed in HuH-7 cells, which was used in the transfection efficiency evaluations. As shown in Fig. 3, no significant cytotoxicity was observed, suggesting safety of our **BHPMs**. Cytotoxicity was further assessed in HUVEC cell-line, which is more sensitive in terms of toxicity [6], and confirmed minimal cytotoxicity was observed with the **BHPMs** at low **H**% (**H**% ≤ 50%). In particular, cytotoxicity was negligible with **H**% ≤ 30%.

In summary, **H** integration conferred multi-merits in elevating transfection efficiency of PEGylated polyplex micelle, including promoted cellular uptake and facilitated endosome escape. Ultimately, **BHPMs** at **B/H** = 70/30 was identified as the most appreciable **BHPM** comprising high transfection efficiency, minimal cytotoxic profile and charge-shielded surface characters for subsequent systemic gene therapy test.

3.3. Potent tumor growth suppression by treatment with BHPMs

Pancreatic cancer remains one of the highest fatalities among various cancers [22–26] and anti-angiogenic approach is recently

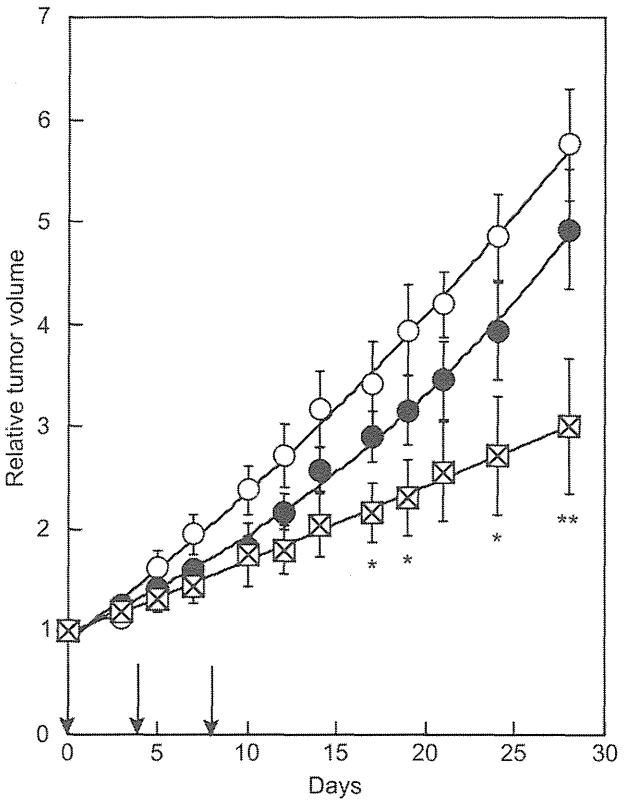

Fig. 5. Antitumor activity of **BHPM** loading sFlt-1 pDNA in subcutaneously BxPC3-inoculated mice via intravenous administration. Open circles: HEPES buffer as control; Closed circles: **B100**; Crossed squares: **BHPM** at **B/H** = 70/30 (mean ± SEM, $n = 6$). Data points marked with asterisks are statistically significance of **BHPM** group relative to both control group and **B100** group (*$P < 0.05$, **$P < 0.01$; Student's t test).

Please cite this article in press as: Chen Q, et al., Homo-catiomer integration into PEGylated polyplex micelle from block-catiomer for systemic anti-angiogenic gene therapy for fibrotic pancreatic tumors, Biomaterials (2012), doi:10.1016/j.biomaterials.2012.03.017

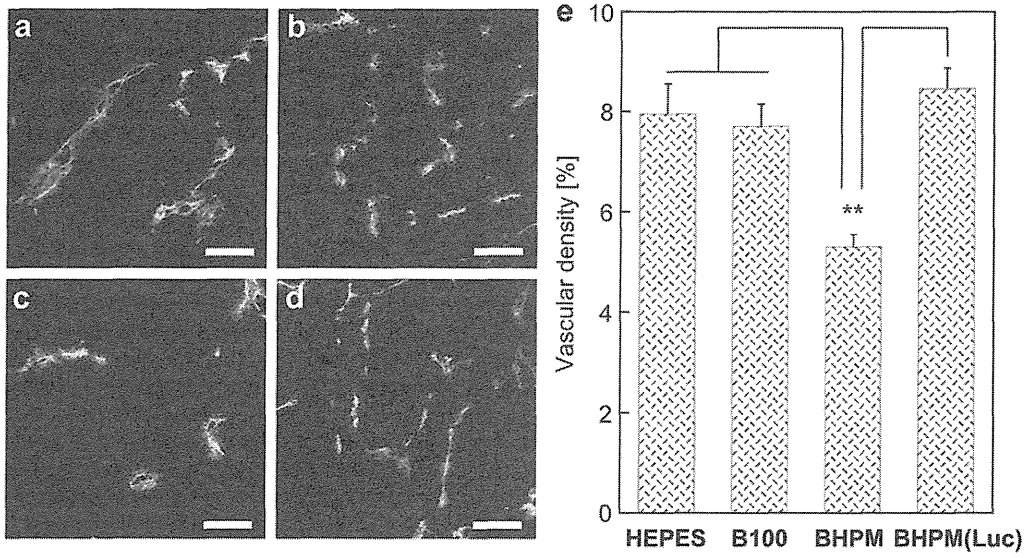

Fig. 6. CLSM image of immunostaining of PECAM-1-positive-vascular endothelial cells in the BxPC3 tumor tissue. a) HEPES; b) **B100** loading sFlt-1 pDNA; c) **BHPM** (**B/H** = 70/30) loading sFlt-1 pDNA; and d) **BHPM** (**B/H** = 70/30) loading Luc pDNA. The scale bars represent 100 μm in all CLSM images. e) Areas of PECAM-1-positive region (green) quantified from CLSM images (mean ± SEM, $n = 15$; $^{**}P < 0.01$, Student's t test). (For interpretation of the references to color in this figure legend, the reader is referred to the web version of this article.)

thought to be a promising way to treat this type of cancer [27,28]. Vascular endothelial growth factor (VEGF), a major signaling molecule to stimulate angiogenesis via promoting endothelial cell proliferation and migration [29,30], is one of most intensively used targets for antiangiogenesis tumor therapy [31–33]. Here, we selected pDNA encoding soluble VEGF receptor-1, or soluble fms-like tyrosine kinase-1 (sVEGFR1, or sFlt-1) [31], which inhibits VEGF signaling by strong binding to VEGF molecules without transducing signals into cells, as payload to test the feasibility of **BHPMs** in systemic applications *in vivo*.

BHPMs at **B/H** = 70/30 (simply referred as **BHPMs** hereafter) containing sFlt-1 were intravenously injected into mice bearing pancreatic adenocarcinoma BxPC3 via the tail vein on day 0, 4 and 8. **BHPMs** exerted significantly tumor suppression compared to the

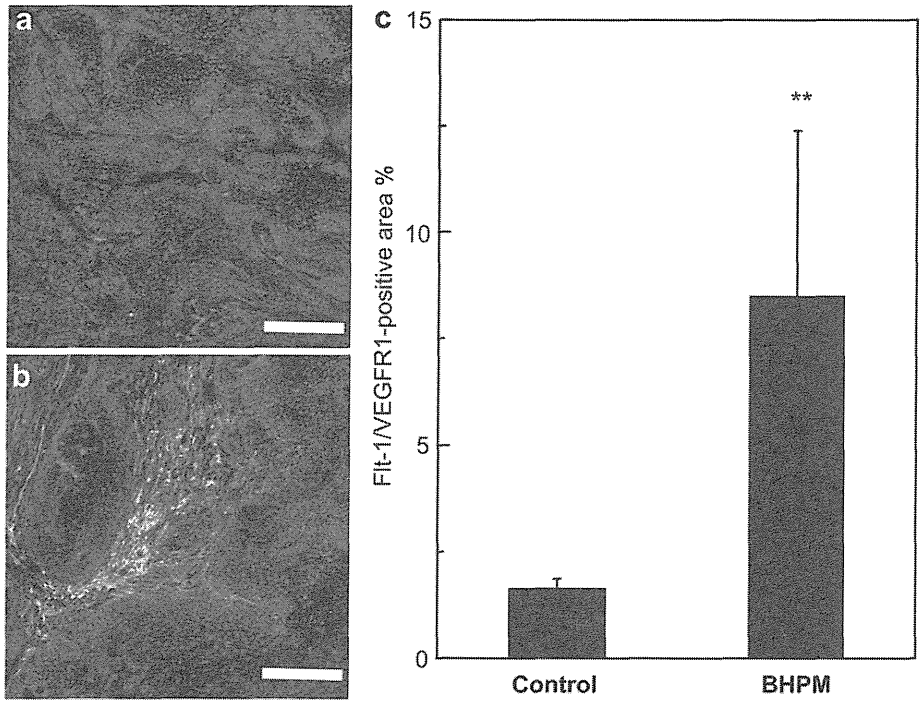

Fig. 7. Expression of sFlt-1 protein by pDNA loaded in **BHPM** (**B/H** = 70/30) in the BxPC3 tumor tissue *in vivo*. a) HEPES buffer used as a control. b) **BHPM** (**B/H** = 70/30) loading sFlt-1 pDNA. Blue: nucleus; Red: vascular endothelial cells. Green: expressed sFlt-1 (or inherent Flt-1/VEGFR1). The scale bars represent 200 μm in all CLSM images. c) Areas of Flt-1/VEGFR1-positive region (green) were quantified from the images (mean ± SEM, $n = 6$; $^{**}P < 0.01$, Student's t test). (For interpretation of the references to color in this figure legend, the reader is referred to the web version of this article.)

Please cite this article in press as: Chen Q, et al., Homo-catiomer integration into PEGylated polyplex micelle from block-catiomer for systemic anti-angiogenic gene therapy for fibrotic pancreatic tumors, Biomaterials (2012), doi:10.1016/j.biomaterials.2012.03.017

mice treated with HEPES buffer (control) and **B100** ($^*P < 0.01$, Fig. 5). Moreover, no noticeable side effect appeared in both **B100** and **BHPMs** treated mice, according to mice weight measurement (data not shown). To confirm the inhibited tumor growth due to anti-angiogenic effect, vascular endothelial cells (VECs) was immunostained by using PECAM-1, and quantified. As shown in Fig. 6, vascular density of tumors treated by **BHPMs** was significantly lower than that of the other groups ($^*P < 0.01$). Note that the vascular density treated by **BHPMs** loading Luc pDNA was the same as the control group. The result suggests the expression of loaded sFlt-1 pDNA in **BHPMs** suppressed vascular growth, thus led to inhibitory growth of tumor tissue.

To confirm obtained anti-angiogenic effect due to loaded sFlt-1 pDNA expression at the tumor site, we immunostained the tumor tissue using an antibody for Flt-1. The antibody detected both soluble and membrane-bound VEGFR1/Flt-1 for both human and mouse, therefore both overexpressed and naturally expressed VEGFR1/Flt-1 in both mouse tissues and human-derived cancer cells were observable. Still, as shown in Fig. 7, the expression of total VEGFR1/Flt-1 (green) was remarkably higher in the mice administered **BHPMs** compared to control sample. This observation suggested that administration of **BHPMs** enabled effective expression of sFlt-1 in the tumor tissue, in agreement with the observations for vascular density decrease (Fig. 6) and tumor growth suppression (Fig. 5). Moreover, it was found that the expressed sFlt-1 enriched in the tumor stroma adjacent to the vascular endothelial cells (red), rather than the tumor mass (cell nucleus stained into blue). Since BxPC3 pancreatic adenocarcinoma has thick fibrosis [34], possibly sFlt-1 pDNA encapsulated in **BHPMs** may have not directly transfected to the cancer cells in the tumor nests, alternatively, it transfected to the stromal cells adjacent to the vascular lumens (e.g. VECs, fibroblasts). The sFlt-1 proteins secreted from these cells might conduce to potent anti-angiogenic environment for the entrapment of VEGF protein in the tumor site, consequently decreased the growth of vascular endothelial cells and retarded the growth of pancreatic tumor. It should be noted that, as opposed to anti-cancer drug, antiangiogenesis gene therapy delineates a particularly fascinating tool due to no necessity of selective and massive transfer of anti-angiogenic genes into all the cancer cells. Namely, transferring anti-angiogenic genes into the cells merely in the vicinity of the tumor site was able to cause spontaneously local accumulation of anti-angiogenic product in the tumor tissue, although not in tumor nests *per se*, resulted in providing adequate anti-angiogenic environment for tumor regression. Since delivering pharmaceutical agent to all the targeted tumor cells is an onerous task, anti-angiogenic tumor therapy is of particular interests and should be an emphasized strategy in treatment for solid tumor.

4. Conclusions

We have demonstrated the utility of **H** integration into **B** based polyplex micelle that potentiates cellular endocytosis and endosome escape for PEGylated polyplex. Furthermore, the most appreciable **BHPM** according to the perspectives of both safety and efficacy was identified toward systemic anti-angiogenic therapy and has validated the feasibility of **H** integration in creating safe and efficient non-viral systemic gene delivery carrier. **BHPM** loaded by sFlt-1 pDNA imparted potent suppression on tumor growth due to inhibitory growth of tumor vascular endothelial cells by the expression of loaded sFlt-1 gene at the tumor site. Therefore, the use of **BHPMs** by strategically integration of **H** is of great interest to promote gene transfection efficiency and worthy to further develop to find broad utility in gene therapy via systemic route.

Acknowledgments

This work was financially supported by the Core Research Program for Evolutional Science and Technology (CREST) from the Japan Science and Technology Corporation (JST), by the Japan Society for the Promotion of Science (JSPS) through its "Funding Program for World-Leading Innovative R&D on Science and Technology (FIRST Program) and by the Center for Medical System Innovation (CMSI) (Global COE Program, MEXT). Q. C. acknowledges the fellowship from Ministry of Education, Science, Sports and Culture, Japan (MEXT). The authors are grateful to Dr. X. Liu for her technical support and assistance in animal experiment and to Ms. Y. Li and Mr. A. Dirisala for their intellectual contributions to the discussion.

Appendix A. Supplementary data

Supplementary data related to this article can be found online at doi:10.1016/j.biomaterials.2012.03.017.

References

[1] Mastrobattista E, van der Aa MAEM, Hennink WE, Crommelin DJA. Artificial viruses: a nanotechnological approach to gene delivery. Nat Rev Drug Discov 2006;5:115–21.
[2] Mintzer M, Simanek EE. Nonviral vectors for gene delivery. Chem Rev 2009; 109:259–302.
[3] Morille M, Passirani C, Vonarbourg A, Clavreul A, Benoit JP. Progress in developing cationic vectors for non-viral systemic gene therapy against cancer. Biomaterials 2008;29:3477–96.
[4] Osada K, Christie RJ, Kataoka K. Polymeric micelles from poly(ethylene glycol)-poly(amino acid) block copolymer for drug and gene delivery. J R Soc Interface 2009;6:S325–39.
[5] Kanayama N, Fukushima S, Nishiyama N, Itaka K, Jang WD, Miyata K, et al. A PEG-based biocompatible block catiomer with high buffering capacity for the construction of polyplex micelles showing efficient gene transfer toward primary cells. Chem Med Chem 2006;1:439–44.
[6] Miyata K, Oba M, Nakanishi M, Fukushima S, Yamasaki Y, Koyama H, et al. Polyplexes from poly(aspartamide) bearing 1,2-diaminoethane side chains induce pH-selective, endosomal membrane destabilization with amplified transfection and negligible cytotoxicity. J Am Chem Soc 2008;130:16287–94.
[7] Itaka K, Ishii T, Hasegawa Y, Kataoka K. Biodegradable polyamino acid-based polycations as safe and effective gene carrier minimizing cumulative toxicity. Biomaterials 2010;31(13):3707–14.
[8] Kim HJ, Ishii A, Miyata K, Lee Y, Wu S, Oba M, et al. Introduction of stearoyl moieties into a biocompatible cationic polyaspartamide derivative, PAsp(DET), with endosomal escaping function for enhanced siRNA-mediated gene knockdown. J Control Release 2010;145:141–8.
[9] Uchida H, Miyata K, Oba M, Ishii T, Suma T, Itaka K, et al. Odd-even effect of repeating aminoethylene units in the side chain of N-substituted polyaspartamides on gene transfection profiles. J Am Chem Soc 2011;133: 15524–32.
[10] Miyata K, Nishiyama N, Kataoka K. Rational design of smart supramolecular assemblies for gene delivery: chemical challenges in the creation of artificial viruses. Chem Soc Rev 2012;41:2562–74.
[11] Nomoto T, Matsumoto Y, Miyata K, Oba M, Fukushima S, Nishiyama N, et al. In situ quantitative monitoring of polyplexes and polyplex micelles in the blood circulation using intravital real-time confocal laser scanning microscopy. J Control Release 2011;151:104–9.
[12] Takae S, Miyata K, Oba M, Ishii T, Nishiyama N, Itaka K, et al. PEG-detachable polyplex micelles based on disulfide-linked block catiomers as bioresponsive nonviral gene vectors. J Am Chem Soc 2008;130:6001–9.
[13] Uchida S, Itaka K, Chen Q, Osada K, Ishii T, Shibata MA, et al. PEGylated polyplex with optimized PEG shielding enhances gene introduction in lungs by minimizing inflammatory responses. Mol Ther; 2012. doi:10.1038/mt.2012.20.
[14] Oba M, Miyata K, Osada K, Christie RJ, Sanjoh M, Li WD, et al. Polyplex micelles prepared from ω-cholesteryl PEG-polycation block copolymers for systemic gene delivery. Biomaterials 2011;32:652–63.
[15] Harada A, Kataoka K. Formation of polyion complex micelles in an aqueous milieu from a pair of oppositely-charged block copolymers with poly(ethylene glycol) segments. Macromolecules 1995;28:5294–9.
[16] Jones MC, Leroux JC. Polymeric micelles - a new generation of colloidal drug carriers. Eur J Pharm Biopharm 1999;48:101–11.
[17] Otsuka H, Nagasaki Y, Kataoka K. Self-assembly of poly(ethylene glycol)-based block copolymers for biomedical applications. Curr Opin Colloid Interface Sci 2001;6:3–10.

Please cite this article in press as: Chen Q, et al., Homo-catiomer integration into PEGylated polyplex micelle from block-catiomer for systemic anti-angiogenic gene therapy for fibrotic pancreatic tumors, Biomaterials (2012), doi:10.1016/j.biomaterials.2012.03.017

[18] Osada K, Oshima H, Kobayashi D, Doi M, Enoki M, Yamasaki Y, et al. Quantized folding of plasmid DNA condensed with block catiomer into characteristic rod structures promoting transgene efficacy. J Am Chem Soc 2010; 132:12343–8.
[19] Mishra S, Webster P, Davis ME. PEGylation significantly affects cellular uptake and intracellular trafficking of non-viral gene delivery particles. Eur J Cell Biol 2004;83:97–111.
[20] Kursa M, Walker GF, Roessler V, Ogris M, Roedl W, Kircheis R, et al. Novel shielded transferrin-polyethylene glycol-polyethylenimine/DNA complexes for systemic tumor-targeted gene transfer. Bioconjug Chem 2003;14: 222–31.
[21] Varkouhi AK, Scholte M, Storm G, Haisma HJ. Endosomal escape pathways for delivery of biologicals. J Control Release 2011;151:220–8.
[22] Mancuso A, Calabrò F, Sternberg CN. Current therapies and advances in the treatment of pancreatic cancer. Crit Rev Oncol Hematol 2006;58:231–41.
[23] Freelove R, Walling AD. Pancreatic cancer: diagnosis and management. Am Fam Physician 2006;73:485–92.
[24] Huguet F, Girard N, Guerche CS. Chemoradiotherapy in the management of locally advanced pancreatic carcinoma: a qualitative systematic review. J Clin Oncol 2009;27:2269–77.
[25] Klautke G, Brunner TB. Radiotherapy in pancreatic cancer. Strahlenther Onkol 2008;184:557–64.
[26] Zuckerman DS, Ryan DP. Adjuvant therapy for pancreatic cancer: a review. Cancer 2008;112:243–9.
[27] Folkman J, Bach M, Rowe JW, Davidoff F, Lambert P, Hirsch C, et al. Tumor angiogenesis-therapeutic implications. N Engl J Med 1971;285:1182–6.
[28] Quesada AR, Munoz-Chapuli R, Medina MA. Anti-angiogenic drugs: from bench to clinical trials. Med Res Rev 2006;26:483–530.
[29] Pralhad T, Madhusudan S, Rajendrakumar K. Concept mechanisms and therapeutics of angiogenesis in cancer and other diseases. J Pharm Pharmaco 2003;55:1045–53.
[30] Carmeliet P, Jain RK. Angiogenesis in cancer and other diseases. Nature 2000; 407:249–57.
[31] Kong HL, Hecht D, Song W, Kovesdi I, Hackett NR, Yayon A, et al. Regional suppression of tumor growth by in vivo transfer of a cDNA encoding a secreted form of the extracellular domain of the Flt-1 vascular endothelial growth factor receptor. Hum Gene Ther 1998;9:823–33.
[32] Oba M, Vachutinsky Y, Miyata K, Kano MR, Ikeda S, Nishiyama N, et al. Antiangiogenic gene therapy of solid tumor by systemic injection of polyplex micelles loading plasmid DNA encoding soluble Flt-1. Mol Pharm 2010;7: 501–9.
[33] Vachutinsky Y, Oba M, Miyata K, Hiki S, Kano MR, Nishiyama N, et al. Antiangiogenic gene therapy of experimental pancreatic tumor by sFlt-1 plasmid DNA carried by RGD-modified crosslinked polyplex micelles. J Control Release 2011;149:51–7.
[34] Cabral H, Matsumoto Y, Mizuno K, Chen Q, Murakami M, Kimura M, et al. Accumulation of sub-100 nm polymeric micelles in poorly permeable tumours depends on size. Nat Nanotech 2011;12:815–23.

Please cite this article in press as: Chen Q, et al., Homo-catiomer integration into PEGylated polyplex micelle from block-catiomer for systemic anti-angiogenic gene therapy for fibrotic pancreatic tumors, Biomaterials (2012), doi:10.1016/j.biomaterials.2012.03.017

Drug Deliv. and Transl. Res. (2012) 2:398–405
DOI 10.1007/s13346-012-0091-1

RESEARCH ARTICLE

Gene transfection to spheroid culture system on micropatterned culture plate by polyplex nanomicelle: a novel platform of genetically-modified cell transplantation

Taisuke Endo · Keiji Itaka · Momoko Shioyama · Satoshi Uchida · Kazunori Kataoka

Abstract Three-dimensional (3D) cellular spheroids have attracted much attention as a transplantation procedure because the increased cell-to-cell interaction in spheroids enhances cell survival and its functions after the transplantation into the body. Furthermore, the potency of spheroidal cells may be further improved by introducing transgenes to augment cellular functions as well as enhance the paracrine effects by secreting key proteins involved in the essential cellular signaling cascades. In this study, we organized a new platform for genetically-modified cell transplantation by combining a microfabricated culture system for 3D spheroid formation with a newly developed non-viral transfection system, polyplex nanomicelle. After transfection of Gaussia luciferase using the nanomicelle, the prolonged luciferase expression was obtained for more than a month with continuous albumin secretion from the hepatocyte spheroids to the level comparable with control spheroids receiving no transfection. In contrast, by the transfection using FuGENE HD, a commercially available lipid-based reagent, the luciferase expression was obtained, yet the albumin secretion was significantly decreased with disintegration of the spheroid architecture. To assess the feasibility of the hepatocyte spheroids for in vivo transplantation, the spheroids were recovered by the use of micropatterned culture plate functionalized with thermosensitive polymer and dispersed into Matrigel™ Matrix. The luciferase expression as well as albumin secretion was maintained for more than a month from the spheroids in the Matrix. Thus, the combination of spheroid cell culture on micropatterned plates with gene introduction using polyplex nanomicelle is a promising platform for genetically-modified cell transplantation to achieve sustained transgene expression with maintaining innate cell functions.

Keywords Cell transplantation · Spheroid · Polyplex nanomicelle · Genetic modification · Micropatterned cell culture

T. Endo · M. Shioyama · K. Kataoka (✉)
Department of Materials Engineering,
Graduate School of Engineering, The University of Tokyo,
7-3-1 Hongo,
Bunkyo-ku, Tokyo 113-0033, Japan
e-mail: kataoka@bmw.t.u-tokyo.ac.jp

K. Itaka (✉) · S. Uchida · K. Kataoka
Division of Clinical Biotechnology, Center for Disease Biology and Integrative Medicine, Graduate School of Medicine,
The University of Tokyo,
7-3-1 Hongo,
Bunkyo-ku, Tokyo 113-0033, Japan
e-mail: itaka-ort@umin.net

Introduction

Cell transplantation is a promising strategy for the treatment of many intractable diseases. Since the therapeutic efficacy of cell transplantation is considered to be chiefly mediated by secreting factors from the transplanted cells [1], a key for successful therapeutic outcome is to find a proper way to keep the transplanted cells in good condition in vivo, leading to sustainable production of major proteinous factors regulating cellular functions [2–4]. In this regard, three-dimensional (3D) cell culture has attracted attention, in which the increased cell-to-cell interaction enhances cell survival and its functions. Particularly, 3D spheroid culture has an advantage to show an accelerated production of regulative proteinous factors and extra cellular matrix compared to monolayer culture system, thereby keeping cells in the condition similar to in vivo situation [5]. Indeed, it is reported by several groups, including ourselves, that the 3D spheroid culture allows not only the enhanced survival of the cells but also the increased cell functions such as

albumin secretion from primary hepatocytes and the multi-lineage differentiation from mesenchymal stem cells [6–12].

Another approach to increase the potency of cell transplantation is the genetic modification of the cells by introducing transgene(s) with either viral or non-viral methods [13]. The cell functions for prolonged survival and differentiation can be augmented by the transgene expressions such as erythropoietin, growth factors, and survival signaling molecules [13, 14]. In addition, the transgene will be capable to secret functional proteins and peptides such as growth factors to enhance the paracrine effects from the cells.

In this study, we applied non-viral gene transfection to 3D spheroid culture systems to induce genetically-modified spheroidal hepatocytes with sustainable function feasible as a platform for future therapeutic application. Obviously the transfection system used for this purpose needs to be non-toxic and effective enough to introduce an external gene for producing proteinous factors in a controlled manner. Here, we applied the polyplex nanomicelle developed in our group as a safe and effective method for gene introduction [15]. This system is composed of plasmid DNA (pDNA) and the block copolymer of poly(ethylene glycol) (PEG) and a cationic segment, poly[N′-[N-(2-aminoethyl)-2-aminoethyl] aspartamide] ([PAsp(DET)]) [16–20]. By mixing of pDNA with this block copolymer in buffer, a micellar structure containing pDNA in a condensed state in the core with surrounding PEG palisade formed spontaneously. This system has high transfection capacity due to the pH-responsive membrane destabilization and eventually enhanced endosomal escaping property motivated by facilitating protonation at endosomal pH of diaminoethane units in the side chain of PAsp(DET) segment [21, 22]. Furthermore, PAsp (DET) is unique in its character to degrade into non-toxic forms under physiological conditions [23]. Thus, this system can minimize cell damage and toxicity incidental to gene introduction, and eventually, prevents the transfected cells from dysfunctions that often occur after the transfection in a time-dependent manner [17, 18].

To evaluate the applicability of this polyplex nanomicelle in 3D spheroid culture, we constructed spheroid arrays from rat primary hepatocytes on the microfabricated culuture plate specially designed for this purpose, followed by the introduction of pDNA encoding a secretory luciferase (Gaussia luciferase) using polyplex nanomicelles to form genetically-modified spheroids. The feasibility of gene introduction by nanomicelles was evaluated by quantifying the amount of secretory luciferase in the medium. Moreover, the albumin secretion was monitored to evaluate the preservation of the innate function of hepatocytes after the gene introduction. Then, to confirm the availability of this system for cell transplantation, the genetically-modified spheroids were transplanted into Matrigel™; the matrix mimicking the in vivo condition, and the sustained secretion of albumin and luciferase were monitored over time.

Materials and methods

Materials

Calcium chloride hydrate ($CaCl_2 \cdot H_2O$), sodium hydrogencarbonate ($NaHCO_3$), collagenase, sodium chloride (NaCl), potassium chloride (KCl), sodium dihydrogen phosphate dehydrate ($NaH_2PO_4 \cdot 2H_2O$), disodium hydrogen phosphate 12-water ($Na_2HPO_4 \cdot 12H_2O$), glucose, dimethylsulfoxide (DMSO), dexamethasone, insulin, and L-proline nicotinamide were purchased from Wako Pure Chemical Industries (Osaka, Japan). 2-[4-(2-hydroxyethyl)-1-piperazinyl] ethanesulfonic acid (HEPES) and ethylene glycol tetraacetic acid (EGTA) were purchased from Dojindo Laboratories (Kumamoto, Japan). Hanks' balanced salt solution and Asc-2P (L-ascorbic acid 2phosphate) were purchased from Sigma-Aldrich (St. Louis, MO, USA). Trypsin inhibitor, Dulbecco's modified eagle's medium (DMEM), and 1 % Pen-Strep-Glut (PSQ) were purchased from GIBCO (Frederich, MD, USA). Human epidermal growth factor (hEGF) was purchased from TOYOBO (Osaka, Japan). Plasmid DNAs (pDNAs) encoding Gaussia luciferase (Gluc) and AcGFP were purchased from New England BioLabs (Ipswich, MA, USA) and Clontech (Madison, WI, USA), respectively, and used after replacement of the promoter to CAG, the combination of cytomegalovirus (CMV) early enhancer element and chicken beta-actin promoter. These pDNAs were amplified in competent DH5α Escherichia coli, and purified using a NucleoBond Xtra Maxi Plus (Takara Bio, Shiga, Japan). A transfection reagent, FuGENE HD, and Renilla Luciferase Assay System were purchased from Promega (Madison, WI, USA). Rat Albumin ELISA Quantitation Set was purchased from Bethyl Laboratories (Montgomery, TX, USA). BD Matrigel™ Basement Membrane Matrix and BD BioCoat™ Cellware six-well Plates were purchased from BD (Frankline Lakes, NJ, USA). PEG-PAsp (DET) block copolymer and PAsp(DET) homopolymer were synthesized as previously reported [16]. The PEG used in this study had a molecular weight of 12,000 and the polymerization degree of the PAsp(DET) portion was determined to be 59 by ^{1}H-NMR. The polymerization degree of the PAsp(DET) homopolymer was determined to be 55 also by ^{1}H-NMR.

Animals

Wister rats (male, 5 weeks old) were purchased from Charles River Laboratories (Yokohama, Japan). All animal protocols were conducted with the approval of the Animal Care and Use Committee of the University of Tokyo, Tokyo, Japan.

Preparation of polyplex nanomicelle

Polyplex nanomicelle was formed by mixing pDNA and polymer solutions that were solved in 10 mM Tris–HCl

buffer (pH 7.4). For preparing the polymer solution, we recently revealed that the combined use of two polymers, PEG-PAsp(DET) block copolymer and PAsp(DET) homopolymer, was advantageous to achieve both effective PEG shielding and functioning of PAsp(DET) to enhance endosomal escape [24]. The nanomicelle has the diameter around 70 nm with almost a neutral zeta-potential of ~+10 mV [25]. Each nanomicelle is loaded with a single pDNA folded regularly into rod-like shape, which was confirmed by transmission electron microscopy [25]. Thus, in this study, we used this type of nanomicelle prepared by mixing pDNA solution with premixed solution of the two polymers at the equal molar ratio of residual amino groups at the N/P ratio (residual molar ratio of total amino groups in the two polymers to phosphate groups in pDNA) of ten. The final pDNA concentration was adjusted to 100 μg/ml for transfection into hepatocyte spheroids.

Isolation and culture of primary hepatocytes

Hepatocytes of male Wistar rats (160–200 g) were isolated by modified two-step collagenase digestion reported previously [26, 27]. Briefly, after the rat liver was perfused from the hepatic portal vein, the collagenase solution was recirculated through the liver to obtain hepatocytes. The hepatocytes were diluted to 4×10^5 cells/ml in the culture medium composed by DMEM medium, 10 % FBS, 1 % PSQ, 1 % DMSO, 10^{-7} mol/l, 1 % PSQ, dexamethasone, 0.5 μg/ml insulin, 10 mmol/l nicotinamide, 0.2 mmol/l Asc-2P, and 10 ng/ml hEGF [28].

For monolayer culture, the hepatocytes were seeded onto 6-well or 24-well culture plates (8×10^5 and 2×10^5 cells/well, respectively) and incubated at 37 °C in a humidified atmosphere containing 5 % CO_2 in the culture medium (1.5 and 400 ml, respectively). Spheroid arrays were formed on novel micropatterned culture plates, in which cell adhesion sites in 100 μm diameter are regularly arrayed in two-dimensional manner surrounded by non-cell adhesive poly (ethylene glycol) (PEG) matrix (Cell-able™ multi-well plate, Transparent, Chiba, Japan). Hepatocyte densities seeded onto the Cell-able™ culture plate were 8×10^5 cells/well in 2 ml culture medium, 4×10^5 cells/well in 1 ml culture medium, and 4×10^4 cells/well in 100 μl culture medium, for 6-, 12-, and 96-well plates, respectively. The cells were incubated for 72 h prior to gene introduction.

In vitro gene introduction to hepatocytes

After the culture medium was replaced with fresh medium, the solution of the polyplex nanomicelles containing 100 μg/ml of pDNA encoding Gaussia luciferase were added to each well at the volume ratio of 1/10 to the culture medium. FuGENE HD was also used for gene introduction by mixing pDNA solutions with FuGENE HD reagent at the weight ratio (reagent/pDNA) of three. The final dose of pDNA was adjusted equal for both FuGENE HD and nanomicelles.

Evaluation of transgene expression of Gaussia luciferase

The Gaussia luciferase is secreted into culture medium and remains stable for more than a week [29]. In this study, to trace the real-time activity of transgene expressions, the culture medium was replaced to fresh medium precisely 24 h prior to each indicated measuring point. Then, the culture medium was collected for the evaluation of luciferase expression during the last 24 h, using a Renilla Luciferase Assay System and a Lumat LB9507 luminometer (Berthold Technologies, Bad Wildbad, Germany) following the manufacturer's protocol.

Enzyme-linked immunosolvent assay (ELISA)

The collected medium was also subjected to the enzyme-linked immunosolvent assays for the evaluation of secreted albumin from hepatocytes, using Rat Albumin ELISA Quantitation Set (Bethyl Laboratories) following the manufacturer's protocol.

Flow cytometry

For the evaluation in transgene expression by a flow-cytometric analysis, the pDNA encoding AcGFP was used. After 24 h of gene introduction, the culture medium was replaced and the cells were incubated for additional 96 h. Then, the cells were washed twice with cold PBS and collected by trypsinization. The AcGFP expression in the resuspended cells in cold PBS was analyzed using a BD™ LSR II flow cytometer (BD Biosciences).

Transplantation of hepatocyte spheroids into Matrigel™

The micropatterned architecture was constructed on the thermosensitive cell culture plates (Upcell™, Cellseed, Tokyo, Japan) to prepare the thermosensitive micropatterned plates for spheroid culture. Cultured spheroids on this plate were recovered as suspension for transplantation study by lowering temperature without any damage in the structure.

Hepatocytes were incubated for 3 days in the wells of the thermosensitive plates to form spheroids. Then, the plates were placed on ice and rinsed with cold PBS, followed by the addition of chilled BD Matrigel™ Basement Membrane Matrix in liquid form to each well. After confirming the spheroid detachment from the substrate, the Matrix in liquid form with dispersed spheroids was collected from the wells and applied to another fresh culture plate for consecutive incubation at 37 °C for 1 day to obtain the Matrix gel with dispersed spheroids.

Results and discussion

Hepatocyte spheroid formation and gene introduction

After seeding primary hepatocytes to the micropatterned culture plate (Cell-able^{TM}), arrays of hepatocyte spheroids were formed corresponding to the micropatterned culture bed of 100 μm diameter (Fig. 1). Transfection was done after a 3-day incubation using either polyplex nanomicelles or FuGENE HD, a commercially available lipid-based transfection reagent, and the expressed Gaussia luciferase as well as albumin secreted from the hepatocytes into the culture medium was quantified simultaneously. Note that we measured albumin secretion as fundamental and essential function of hepatocytes to evaluate whether cells are in good vital condition because there is a good correlation between the ability of albumin secretion and vital status of hepatocytes. The luciferase expression was observed on the next day of transfection by the polyplex nanomicelle and continuously detected for more than a month (Fig. 2a). The albumin secretion was also maintained similarly as the control spheroids without receiving transfection, indicating that the nanomicelle has minimum adverse impact on hepatocyte function (Fig. 2b). When using FuGENE HD, the luciferase expression was in a similar extent as nanomicelle case, however, albumin secretion showed a remarkable decrease even after 2 days of transfection. Furthermore, the spheroids were mostly disintegrated one day after the FuGENE HD transfection (Fig. 3b), indicating a substantial damage to cell-to-cell adhesion functions even Gaussia luciferase expression was continuously observed.

Identification of major cell types undergoing transgene expression

Primary hepatocytes collected by the collagenase digestion performed in this study contain small non-parenchymal cells as well as larger parenchymal cells that secrete albumin [30].

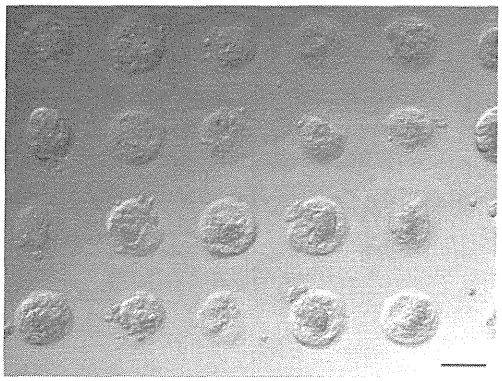

Fig. 1 Hepatocyte spheroids three days after the seeding of primary hepatocytes onto the micropatterned culture plate. *Bars*=100 μm

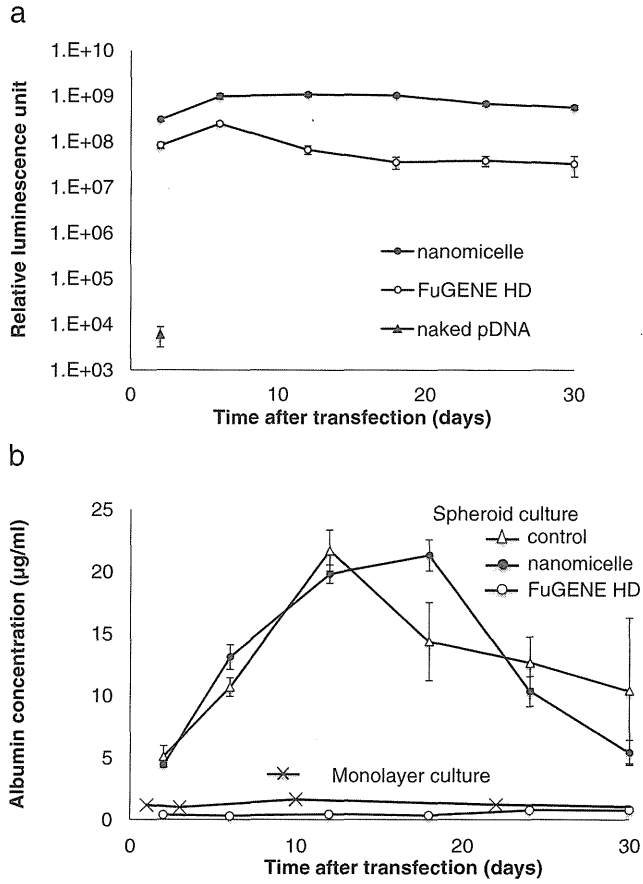

Fig. 2 **a** Transgene expression of Gaussia luciferase after transfection to hepatocyte spheroids using polyplex nanomicelle, FuGENE HD, or naked pDNA. **b** Albumin secretion from hepatocytes spheroids or hepatocytes in monolayer culture. Spheroids received transfection by nanomicelle or FuGENE HD. The albumin secretion from control hepatocytes (in spheroids or monolayer culture) without receiving transfection was also represented. Results are means±SEM, n=4 for monolayer culture and n=6 for spheroids, respectively

Thus, we need to identify the cell types mainly undergoing transgene expression by polyplex nanomicelle. To get insight into this issue, pDNA encoding AcGFP gene was transfected to the spheroids by polyplex nanomicelle. Then the flow-cytometric (FCM) analysis was done after trypsinization of the spheroids to single cell, in order to examine the transgene expression in each subgroup of parenchymal and non-parenchymal cells that can be discriminated by cell size.

For smaller cell population corresponding to non-parenchymal cells, the cell distribution in the intensity histogram of GFP fluorescence showed a clear upper shift to the right after the transfection (Fig. 4a), indicating the GFP expression in a considerable number of non-parenchymal cells. The change in the histogram after the transfection of the larger-sized cell population, mainly consisted with parenchymal cells, was not clear due to the considerably high autofluorescence from the cells, and thus, the efficacy of transfection to parenchymal cells was yet to be confirmed (Fig. 4b).

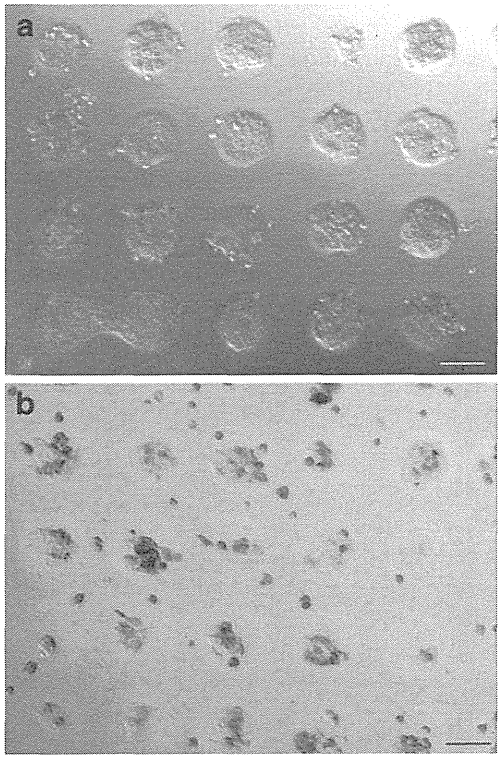

Fig. 3 Hepatocyte spheroids a day after the gene transfection using polyplex nanomicelle (**a**) or FuGENE HD (**b**). *Bars*=100 μm

The FCM analysis was unavailable for detection of GFP after transfection using FuGENE HD because the cell number was significantly decreased after the transfection as indicated by the disintegration of spheroids (Fig. 3b). However, even in this case, cumulative luciferase expression was maintained as almost the same level as the spheroids transfected by the nanomicelles (Fig. 2a). Careful observation by the microscopy of the cells that were still remaining on the plate after FuGENE HD transfection revealed that the major fraction of the observed cells apparently belonged to small cell population. It is thus likely that observed expression of luciferase in FuGENE HD transfected system may chiefly be derived from the small non-parenchymal cell population. However, most of the parenchymal cell population was lost due to the disintegration of spheroids, resulting in the significant decrease in albumin secretion as seen in Fig. 2b.

The reason of the spheroid disintegration observed in FuGENE HD transfected system may be the membrane destabilization induced by FuGENE HD. The transfection reagents based on cationic lipids such as FuGENE HD are known to induce membrane destabilization to facilitate the internalization of the lipoplexes into cells [31, 32]. It should be noted that the change in cell membrane is likely to be transient and recoverable, not inducing the cell death. Indeed, as shown in Fig. 2a, the luciferase expression was maintained for almost a month after the transfection using FuGENE HD, strongly suggesting the survival of the luciferase-expressing cells. However, for the spheroids where the cell-to-cell contact plays an important role in maintaining the structure, the perturbation in the membrane integrity, even transient, is likely to deteriorate cell-to-cell contact, resulting in the disintegration of the spheroids, and eventually the decrease in albumin secretion (Fig. 2b).

In a sharp contrast to FuGENE HD, the polyplex nanomicelle is unique to maintain the spheroid architecture during transfection, leading to appreciably high transgene expression as well as sustainable albumin production comparable to control spheroids receiving no transfection. The

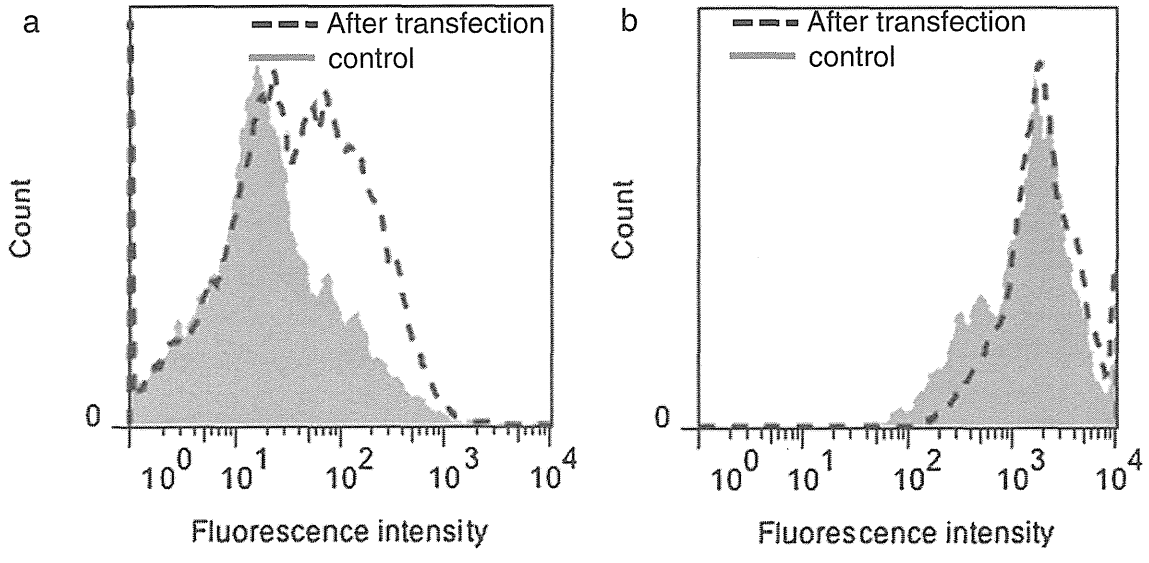

Fig. 4 Flow-cytometric analyses after transfection of AcGFP gene by polyplex nanomicelle. The cells in spheroids were isolated by trypsinization and subjected for flow cytometry for each subgroup of non-parenchymal (**a**) and parenchymal cells (**b**) that can be discriminated by cell size. The data were represented by histograms of the fluorescent intensity corresponding to GFP

nanomicelle-transfection system was thus feasible to introduce a transgene to produce genetically-modified spheroids with maintaining the innate functions of spheroidal cells. Possibly due to the PEG shell layer, the nanomicelles were revealed previously to percolate deep into the spheroid interior [33], and this may also be a factor contributing to increase the transfection efficiency.

Transplantation of hepatocyte spheroids into Matrigel™

To assess the feasibility of hepatocyte spheroids for in vivo transplantation, we evaluated luciferase expression and albumin secretion after the spheroids were transplanted into BD Matrigel™ Basement Membrane Matrix, a model gel matrix mimicking the physiological conditions inside the body. As described in the "Materials and methods" section, the spheroids were successfully dispersed in the liquid form of the chilled Matrigel™ Matrix using the thermosensitive micropatterned plates. Even after the gelation of the Matrix, the hepatocyte spheroids could indeed survive inside of the Matrix with maintaining their original architecture (Fig. 5a). Notably, the luciferase expression stably continued for more than a month from the Matrix-embedded spheroids receiving transfection by polyplex nanomicelle (Fig. 5b), with an enhanced secretion of albumin into the culture medium over time comparable to the control spheroids receiving no transfection (Fig. 5c). This increase in albumin secretion indicates sustainable function of embedded spheroids, even after receiving nanomicelle transfection, in the Matrigel™ Matrix containing growth factors.

It should be noted that hepatocyte spheroids are usually prepared by co-culture with feeder cells, such as endothelial cells, because the feeder cells contribute to stabilize spheroid structure, eventually sustaining the functions of constituent hepatocytes [34]. However, in this study, we avoided the use of feeder cells in spheroid formation because the

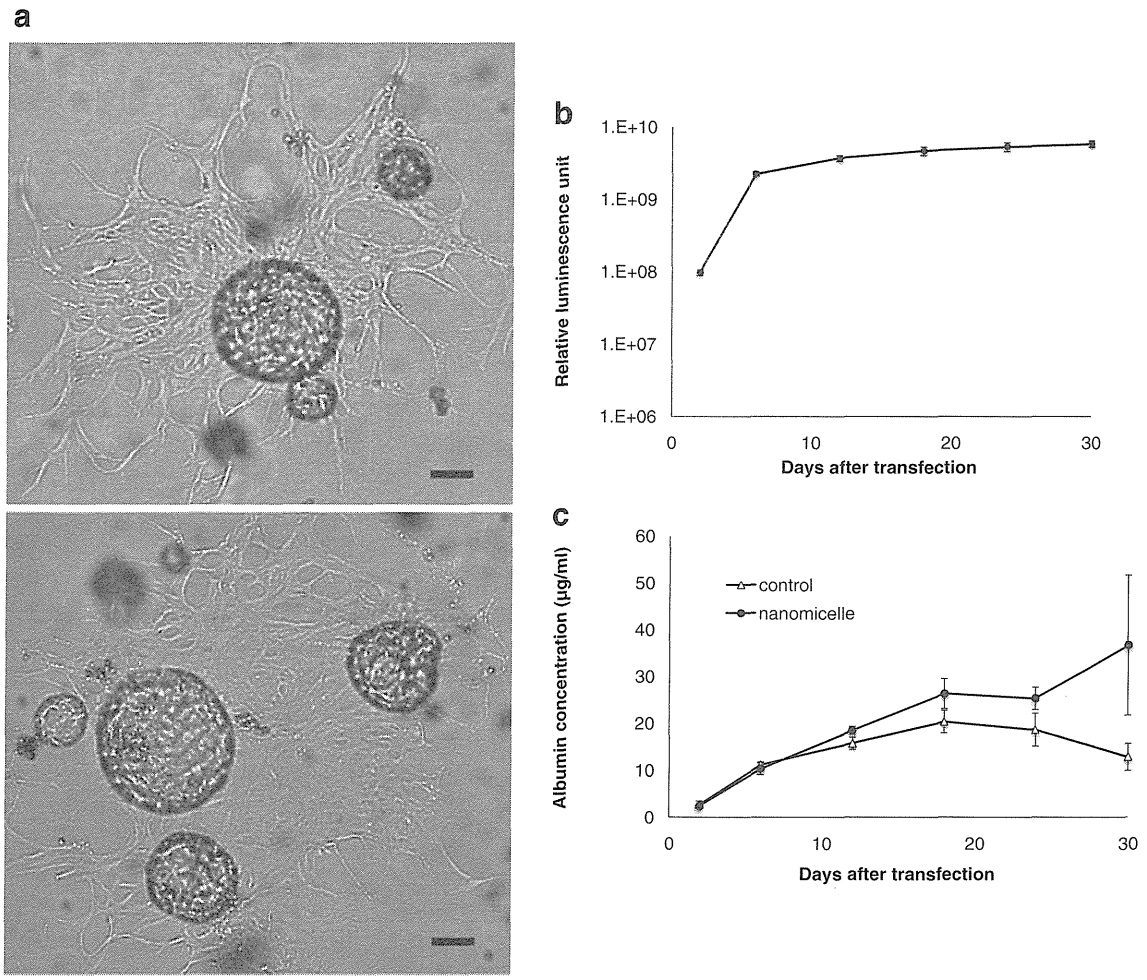

Fig. 5 Hepatocyte spheroids after the transplantation into Matrigel (BD Matrigel™ Basement Membrane Matrix). **a** Spheroids inside Matrigel after 30 days of transplantation. *Above* Spheroids subjected to the gene transfection by polyplex nanomicelle. *Below* Control spheroids without receiving transfection. *Bars*=100 μm. **b** Transgene expression of Gaussia luciferase from the transplanted spheroids. **c** Albumin secretion from the transplanted spheroids. Results are means±SEM, $n=3$

heterogeneous cell source was not suitable for certain aspects of transplantation. Consequently, the optimum culture condition to form spheroid array on Cell-able^{TM} plate was successfully established without using the feeder cells, yet recovery of intact spheroids from the plate was another issue because procedures such as trypsinization and mechanical scratching might impair the structure and function of spheroids. Thus, we solved this issue by newly developing the micropatterned plate having arrayed wells immobilized with thermosensitive polymer, poly(iso-propylacrylamide) (PIPAAm), which are widely used in the thermoresponsive cell recovery system [35–37]. Another note which might be worthy to mention is that the spheroid formation became inefficient with irregular shape after purifying the hepatocytes by removing non-parenchymal cells with low-speed centrifugation (data not shown). Thus, it is likely that the non-parenchymal cells may play a similar role as feeder cells to stabilize the spheroid structure on the micropatterned plates, and even after transplanted into Matrigel^{TM}.

It is demonstrated that the hepatocyte spheroids on the thermosensitive micropatterned culture plates were successfully recovered for cell transplantation after gene transfection by the polyplex nanomicelle. The transgene expression as well as the major hepatic function of albumin secretion was maintained for more than a month after spheroid transplantation into Matrigel^{TM}. These achievements are now directing us to investigate in vivo transplantation of spheroids for animal disease models after transfection of therapeutic transgenes by polyplex nanomicelles. The results will be reported elsewhere in near future.

Conclusion

In this study, the feasibility of gene introduction using polyplex nanomicelle was investigated for the spheroids of primary hepatocytes on the micropatterned culture plates. After transfection to spheroids using the nanomicelle, the prolonged transgene expression was obtained for more than a month. During the transfection, albumin secretion from the hepatocyte spheroids was maintained to the level comparable with control spheroids receiving no transfection. Moreover, the spheroids were successfully recovered without any damage in the architecture by the use of micropatterned culture on newly developed thermosensitive plates. After transplantation of the spheroids into Matrigel^{TM} Matrix, the transgene expression as well as albumin secretion was maintained for more than a month. Thus, the combination of spheroid cell culture on micropatterned plates with gene introduction using polyplex nanomicelle is a promising platform for genetically-modified cell transplantation to achieve sustained transgene expression with maintaining innate cell functions.

Acknowledgments We deeply appreciate Dr. Takeshi Ikeya and Mr. Seiki Uozaki (Transparent Inc. Chiba, Japan) for providing thermosensitive Cell-able^{TM} micropatterned culture plates, as well as various scientific advices. We also thank Ms. Satomi Ogura and Ms. Katsue Morii (The University of Tokyo) for technical assistance of collecting primary hepatocytes from rats. This work was financially supported in part by the Core Research Program for Evolutional Science and Technology (CREST) from Japan Science and Technology Corporation (JST) (K. K.), Grants-in-Aid for Scientific Research form the Japanese Ministry of Education, Culture, Sports, Science and Technology, Japan (MEXT) (K. I.), Global COE Program "Medical System Innovation through Multidisciplinary Integration" from MEXT, Japan.

References

1. Lavasani M, Robinson AR, Lu A, Song M, Feduska JM, Ahani B, et al. Muscle-derived stem/progenitor cell dysfunction limits healthspan and lifespan in a murine progeria model. Nat Commun. 2012;3:608.
2. Takemura T, Kondo S, Homma T, Sakai M, Harris RC. The membrane-bound form of heparin-binding epidermal growth factor-like growth factor promotes survival of cultured renal epithelial cells. J Biol Chem. 1997;272(49):31036–42.
3. Clark WA, Decker ML, Behnke-Barclay M, Janes DM, Decker RS. Cell contact as an independent factor modulating cardiac myocyte hypertrophy and survival in long-term primary culture. J Mol Cell Cardiol. 1998;30(1):139–55.
4. Yasui K, Kada K, Hojo M, Lee JK, Kamiya K, Toyama J, et al. Cell-to-cell interaction prevents cell death in cultured neonatal rat ventricular myocytes. Cardiovasc Res. 2000;48(1):68–76.
5. Kelm JM, Fussenegger M. Scaffold-free cell delivery for use in regenerative medicine. Adv Drug Deliv Rev. 2010;62(7–8):753–64.
6. Landry J, Bernier D, Ouellet C, Goyette R, Marceau N. Spheroidal aggregate culture of rat liver cells: histotypic reorganization, biomatrix deposition, and maintenance of functional activities. J Cell Biol. 1985;101(3):914–23.
7. Yuasa C, Tomita Y, Shono M, Ishimura K, Ichihara A. Importance of cell aggregation for expression of liver functions and regeneration demonstrated with primary cultured hepatocytes. J Cell Physiol. 1993;156(3):522–30.
8. Otsuka H, Hirano A, Nagasaki Y, Okano T, Horiike Y, Kataoka K. Two-dimensional multiarray formation of hepatocyte spheroids on a microfabricated PEG-brush surface. ChemBioChem. 2004;5(6):850–5.
9. Wang W, Itaka K, Ohba S, Nishiyama N, Chung UI, Yamasaki Y, et al. 3D spheroid culture system on micropatterned substrates for improved differentiation efficiency of multipotent mesenchymal stem cells. Biomaterials. 2009;30(14):2705–15.
10. Bartosh TJ, Ylostalo JH, Mohammadipoor A, Bazhanov N, Coble K, Claypool K, et al. Aggregation of human mesenchymal stromal cells (MSCs) into 3D spheroids enhances their antiinflammatory properties. Proc Natl Acad Sci U S A. 2010;107(31):13724–9.
11. Frith JE, Thomson B, Genever PG. Dynamic three-dimensional culture methods enhance mesenchymal stem cell properties and increase therapeutic potential. Tissue Eng Part C Meth. 2010;16(4):735–49.
12. Nakasone Y, Yamamoto M, Tateishi T, Otsuka H. Hepatocyte spheroids underlayered with nonparenchymal cells for biomedical applications. IEICE Trans Electron. 2011;E94(C(2)):176–80.
13. Haider H, Mustafa A, Feng Y, Ashraf M. Genetic modification of stem cells for improved therapy of the infarcted myocardium. Mol Pharm. 2011;8(5):1446–57.